

## Secure Medical Data Transmission: An Adversarial Neural Cryptography-Based Steganography Technique with Digital Signature and LSB Replacement

Gulfam Ahmad<sup>1</sup>, Fatima Gulzar<sup>2</sup>, Hina Riaz<sup>3</sup>

<sup>1</sup>, Ghazi University, Dera Ghazi Khan [hahmad@gudgk.edu.pk](mailto:hahmad@gudgk.edu.pk)

<sup>2</sup>, Ghazi University Dera Ghazi Khan Email: [fgulzar@gudgk.edu.pk](mailto:fgulzar@gudgk.edu.pk) Corresponding author: Fatima Gulzar

<sup>3</sup>, Department of CS&IT Ghazi University, Dera Ghazi Khan, Pakistan

### Abstract

It is difficult to secure sensitive healthcare data in light of current technological advancements. Protecting medical material, including patient privacy, is one of the most important concerns with medical information security. In order to safeguard confidentiality, integrity, and availability, security measures must be put in place as medical information becomes increasingly accessible. Recently, image steganography was suggested as an additional data security measure for medical information. This study describes a data-hiding strategy for DICOM medical images. In order to maintain confidentiality, we encrypt and hide the RGB patient image within the Region of Non-Interest (RONI) of the medical image using Adversarial Neural Cryptography with SHA-256 (ANC-SHA-256). Before embedding, we encrypt the RGB patient picture using ANC-SHA-256 to guarantee anonymity. To verify the integrity and authenticity of medical images, we use a secure hash technique with 256 bits (SHA-256) to create a digital signature from the data associated with the DICOM file. Using a variety of medical datasets, such as MRI, CT, X-ray, and ultrasound cover images, several tests were carried out to evaluate visual quality. As a patient-concealed image, the LFW dataset was used. In terms of visual quality metrics, such as the PSNR average of 67.55, the NCC average of 0.9959, the SSIM average of 0.9887, the UQI average of 0.9859, and the APE average of 3.83, the suggested approach works well. In six medical evaluation categories, it performs better than the state-of-the-art methods in these visual quality metrics (PSNR, MSE, and SSIM). Additionally, the suggested approach provides excellent visual quality while withstanding geometrical threats like cropping, rotation, and scaling, as well as physical changes and histogram analysis. Lastly, its high attaining security ratio of 99% during remote transmission of Electronic Patient Records (EPR) via the Internet makes it especially effective in telemedicine applications, protecting patient privacy and data integrity.

**Keywords:** Secure Medical, Data Transmission, Adversarial Neural Cryptography,

### 1. Introduction

There has been an increase in the need for secure techniques to preserve patient privacy and maintain data integrity as a result of the growing digitalization of medical records and the widespread usage of digital imaging and communications in medicine (DICOM) pictures (Qiu et al., 2023). The protection of patient confidentiality is of the utmost importance in the medical industry, as any violation of confidentiality may result in serious repercussions for both patients

and healthcare individuals. In this paper, a new data-hiding method that was developed exclusively for DICOM medical pictures is presented. This technique makes use of Adversarial Neural Cryptography in conjunction with SHA-256 (ANC-SHA-256) to encrypt and hide RGB patient images inside the Region of Non-Interest (RONI) of the medical images. Not only does this strategy guarantee that sensitive information is not discovered among the vital medical information, but it also ensures that the confidentiality of patient data is maintained (Alhassan, 2023). In order to provide an extra degree of security that protects against unwanted access and guarantees that only authorized individuals are able to obtain and see the secret data, the RGB patient picture is encrypted using ANC-SHA-256 before the embedding process. Through the use of a secure hashing algorithm known as SHA-256, it is possible to generate a digital signature that is connected to the DICOM file. This digital signature serves the purpose of certifying the validity and integrity of the medical pictures itself. This element is also important in the field of medicine, where the precision and dependability of pictures may have a considerable influence on the choices that are made about diagnosis and treatment (Wang et al., 2017). In order to determine whether or not this suggested technique is beneficial, thorough testing was carried out on a variety of medical datasets, which included MRI, CT, X-ray, and ultrasound cover pictures. The performance measures showed remarkable results, with the average Peak Signal-to-Noise Ratio (PSNR) reaching 67.55 dB, the Normalized Cross-Correlation (NCC) averaging 0.9959, and the Structural Similarity Index (SSIM) averaging 0.9887. All of these metrics were remarkable. Based on these measures, it can be concluded that the quality of the stego pictures, which are the photos that have been embedded, continues to be extraordinarily great, with just a small amount of distortion being noticeable. Further evidence that the suggested strategy is successful in preserving visual quality is provided by the Universal Quality Index (UQI) and the Average Pixel Error (APE), both of which averaged out to be 0.9859 and 3.83, respectively. Our technique displays improved performance in six different medical assessment categories when compared to the approaches that are currently considered to be state-of-the-art. This is especially relevant when it comes to visual quality measurements like PSNR, Mean Squared Error (MSE), and SSIM. This study makes a major contribution to the continuing efforts to improve security procedures in medical imaging, eventually leading to a better level of confidence in digital healthcare solutions. This is accomplished by protecting the confidentiality and integrity of patient data. There are two emerging topics: picture steganography and multimedia security. In each of these domains, data is concealed inside an image in such a way that it may be seen or not seen. It has previously been accomplished in the frequency domain as well as the spatial domain (Gholami et al., 2020). By adjusting the values of the pixels directly in the spatial domain, the secret message may be concealed. The majority of the most current safe steganographic methods for digital pictures that are represented in the spatial domain are content-adaptive. The result of this is that steganography can alter the embedding process in intricate sections of the cover picture, which are notoriously difficult to identify. It is anticipated that this will lead to an enhancement in the level of multimedia security against steganographic analysis attackers (Cai et al., 2019). Steganography methods in the spatial realm are quite straightforward because the information that is being concealed is immediately included in the values of the pixels. The integration of digital signatures with steganography markedly improves the integrity and validity of concealed information, especially in critical domains such as medical imaging. A digital signature involves a cryptographic method that leverages a private key to provide a distinctive identifier for a data set. This identity, or signature, may be authenticated by a matching public key (Hua et al., 2023). The use of digital signatures in steganography fulfills many functions: it facilitates integrity verification by allowing the original material to be signed before embedding, so assuring that any subsequent extraction

operation can confirm whether the data has been modified. Moreover, digital signatures authenticate the concealed data, ensuring that the retrieved information comes from a credible source. This approach promotes confidence and accountability since the sender cannot subsequently deny having sent the signed data, thereby ensuring non-repudiation in steganographic communications. The use of steganography in medical imaging encounters certain constraints. A significant problem exists in the balance between capacity and imperceptibility; excessive data embedding may result in discernible changes to medical picture quality, thereby undermining diagnostic efficacy. Moreover, medical pictures often undergo diverse processing procedures, including compression or scaling, which may unintentionally obscure latent information. Advanced steganalysis algorithms may identify modifications, rendering the concealed data susceptible to revelation. The intricacy of merging adversarial neural cryptography with steganography and digital signatures may provide issues in deployment and maintenance, especially in resource-limited medical settings where substantial computer power is required for neural cryptography models. This work introduces an innovative medical steganography strategy that integrates two authentication factors—encryption and digital signatures—utilizing the Histogram of Oriented Gradients (HOG) and Least Significant Bit (LSB) methods to conceal information. The suggested technique entails segmenting the medical picture into Regions of Interest (ROIs) and Regions of Non-Interest (RONIs), with RONIs identified using computed gradient magnitudes and a specified threshold value (T). By modifying essential parameters (K and T), the embedding rate may be refined according to the dimensions of the Electronic Patient Record (EPR) to guarantee that the RONIs can flexibly include concealed information. The patient's picture is encrypted using the ANC SHA-256 method prior to its embedding in the LSB of the RONIs. The method transforms information from the DICOM file into a digital signature using SHA-256 and a private key on the sender's side. Upon receipt of the data, the receiver retrieves the digital signature using the public key, contrasts hash values obtained from both the DICOM file and the embedded data, and verifies the absence of alterations.

## 2. Literature review

There are a number of advantages associated with telemedicine, including the enhancement of access to medical information, the provision of treatment, and the identification of the diagnostic that is the most cost-effective (Yang et al., 2012). The low-security level of the medical information that is transferred and the poor quality of the medical pictures that are received are two of the difficulties that telemedicine must contend with, despite the fact that it has previously shown a number of benefits. Within DICOM image formats, the EPR is represented as metadata, which is comprised of a collection of pixels. Additionally, the header contains information that connects the picture to the EPR that corresponds to it. In this manner, developments in the technologies of telecommunications have resulted in the proliferation of services that are based on DICOM files for the transmission of medical pictures via Picture Archiving and Communication Systems (PACS), which is a technology that adheres to the DICOM standard. PACS also makes it possible to build a variety of applications, such as telemedicine and the capacity to diagnose patients remotely, amongst others. Additionally, propose the steganographic method known as SCRIPT, which is built on pictures and prompts that are created simultaneously by the shaRing device. Through the process of locating robust coefficients inside the picture for message embedding and synchronizing their placements, this method allows for acceptable levels of security and resilience. Similarly, suggested the soft lossless compression technique for the purpose of recovering accuracy and hiding invisibility. This was accomplished by using a natural target picture in order to disguise the hidden medical image with the QR code for the patient

diagnostic information (PDI). This resulted in the integration of blockchain technology, which improved data security and verification of its integrity. A region-based medical picture encryption has been developed by (Rajak & Shaw, 2019). This encryption method makes use of a two-dimensional logistic sine map (2DLSM) and an advanced zigzag transform to ensure the safety of medical images. The proposed method is thus effective in guarding against a wide variety of assaults and has the potential to provide a satisfactory and secure return on investment for a variety of medical photographs, considering their varying sizes and kinds. EPR may be discovered by unauthorized persons who attempt to access patient information despite the digital signature and encryption techniques that are used in DICOM pictures. The implementation of steganography technology has been crucial in the development of telemedicine applications since it has enabled the provision of privacy, integrity, and uniqueness. In the field of telemedicine, the Internet and other cloud computing technologies that have emerged in recent years have been used extensively to provide a variety of medical treatments to patients who are located in distant territories. In order to provide a variety of medical treatments to patients who are located in distant areas, telemedicine has been using an increasing number of technologies. There are a number of advantages that come about as a result of the use of these apps, including enhanced accessibility to medical information, the development of care delivery, and more economical diagnostics. Telemedicine has a number of important downsides, including the degree of confidentiality of medical information that is sent and the quality of medical pictures that are received. These difficulties are despite the fact that telemedicine provides those benefits described above. The data pertaining to the patient needs to be kept confidential, and the transmission of medical information ought to be a secure process. Improved embedding capacity may be achieved via the use of a variety of adaptive steganographic approaches. An adaptive LSB technique was described by (Andritsos & Tang, 2014). This method makes use of the random k-bit embedding approach. This technique takes advantage of the correlation between surrounding pixels and was developed suggested a novel method for RGB photos that makes use of the characteristics of the host image in an adaptive manner to conceal a greater amount of information than there is in other places. For the purpose of including confidential information, the LSB replacement strategy was used. The capacity has been increased, and an undetectable stego-image quality has been attained; nevertheless, there is a significant downside in terms of the complexity of the computations and the amount of time it takes to execute. Recent research conducted suggested that the fuzzy logic technique might be used to conceal secret bits while also providing a large payload and excellent imperceptibility. The most important premise is to locate edge regions that are able to accommodate a greater number of embedding bits than smooth areas, as determined by HVS parameters. In order to enhance the safety of medical photographs, a number of different strategies have been presented. For example, provided a framework for medical imaging that is both secure and of good visual quality. For the purpose of protecting patients' privacy and enhancing picture quality, they proposed a technology known as reversible data hiding (RDH), which is based on lesion extraction and embeds confidential information into medical images. Additionally, in order to ensure multimedia security, pictures are encrypted using a method known as homomorphic encryption. Suggested a pixel similarity-based LSB approach that is based on optimal pixel selection for the purpose of concealing personal medical information pertaining to patients. For the purpose of preserving robustness and visual quality in accordance with MSE, RMSE, PSNR, and SSIM, the medical pictures have concealed capacities that range between 5,000 and 10,000 characters. Recently, presented a demonstration of the suggested method known as zero-steganography, which is intended for the transfer of medical images across communication channels that are not secure. By achieving good resilience against assaults such as filtering, compression, and the injection of noise, it protects itself well. Magdy,

presented a variety of security methods, including steganography, cryptography, and watermarking, among others. Additionally, introduced a novel data-hiding strategy that makes use of medical DICOM pictures in order to retain high levels of resilience. Provided a technique for safeguarding medical pictures by using chaotic map encryption and LSB. This approach was developed within the same particular domain. They improve both the security and the visual quality of the image by combining the Triple Data Encryption Algorithm (3DES) and the Advanced Encryption Standard (AES) with three chaotic maps. The researchers suggested a high-quality safe approach that makes use of LSB replacement to conceal secret bits inside medical pictures. The goal of this technique is to boost capacity while keeping their security. It is recommended that a combination of HOG-LSB and ANC SHA-256 techniques be used in order to verify two authentication factors: encryption and digital signatures. The HOG-LSB strategy is used for the purpose of concealing metadata and enhancing the safety of medical pictures. The use of digital signatures in steganography methods promotes trust in the integrity and validity of the information that is concealed while simultaneously ensuring privacy and the security of medical information. Extensive studies have been carried out on medical photographs, and the results show that the proposed approach is both practicable and successful.

### 3. Adversarial neural cryptography with SHA-256 encryption

The methodology that we have presented makes use of a highly nonlinear image encryption method known as ANC, which is paired with SHA-256. This allows us to successfully defend against common assaults, such as differential attacks that target patient photos (Li et al., 2020). The adversarial neural cryptography and chaotic systems that are used in this technique are shown in Figure 1. Alice, Bob, and Sam are the three individuals who may be found within the ANC framework. In this scenario, Alice and Bob have a shared secret key, which is denoted by the letter  $K$ , and they want to convey their message, denoted by the letter  $M$ , confidentially. As part of the Artificial Neural Network (ANC) architecture, the neural networks that Alice and Bob have created serve as the generator in a Generative Adversarial Network (GAN), which is represented by the notation  $G(M)$   $G(M)$ , on the other hand, Sam's neural network is the discriminator, which is represented by the notation  $D(M)$   $D(M)$ . The encryption process is essentially the responsibility of Alice's network, whereas Bob's network is in charge of the decryption aspect of the process. The fact that Sam is unable to decode the message without having access to the key is a significant factor that contributes to the increased safety of the relationship. An illustration of the picture encryption and decryption processes may be seen in Figures 2 and 3, respectively. In this particular system, the parameters  $\alpha$  and  $\beta$  are used as cipher keys. More precisely, the value  $\alpha$  corresponds to the initial value  $x_0$  in Equation (1), while the value  $\beta$  corresponds to the starting value  $x_0$  in Equation (2). This powerful combination of SHA-256 and Artificial Neural Networks (ANC) guarantees a high degree of protection for patient photos against any possible attacks.

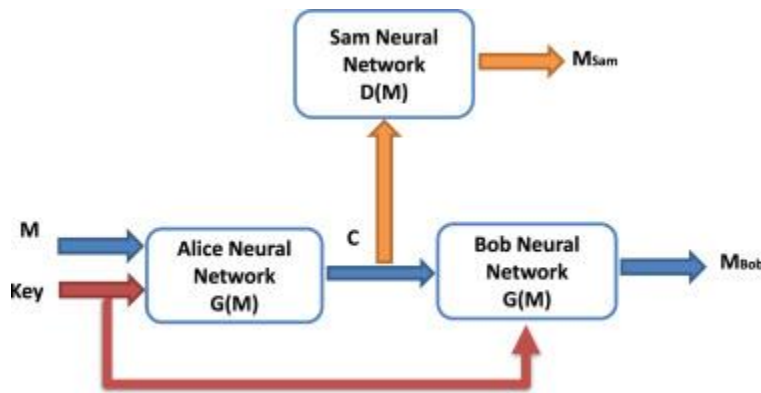


Fig. 1. The Adversarial Neural Cryptography framework.

An additional point to consider is that a logistic map is a well-known example of a classical chaotic dynamic system that generates chaotic sequences that exhibit stable features. It is possible to explain it in the following manner.

$$x_{n+1} = \mu x_n(x_n + 1), x_0 \in (0,1) \quad (1)$$

$$x_{n+1} = [\mu x_n(1 - x_n) + (4 - \mu)\sin(\pi x_n)/4] \bmod 1 \quad (2)$$

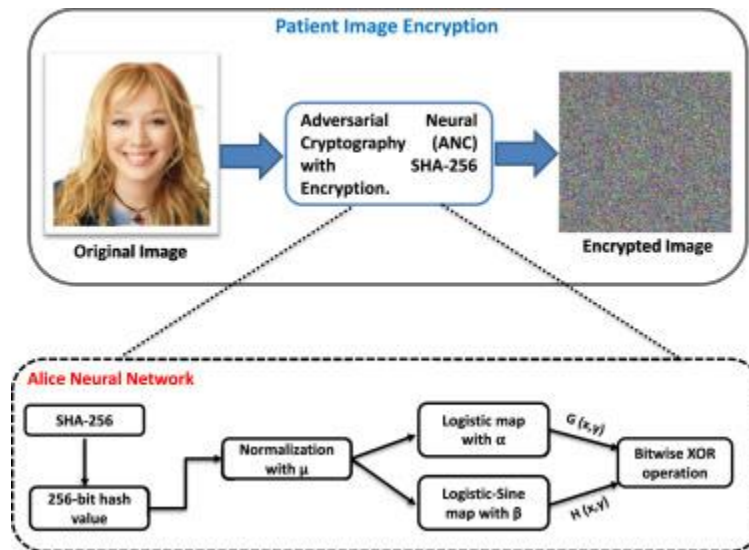


Fig. 2. ANC and SHA-256 are used in the patient picture encryption process.

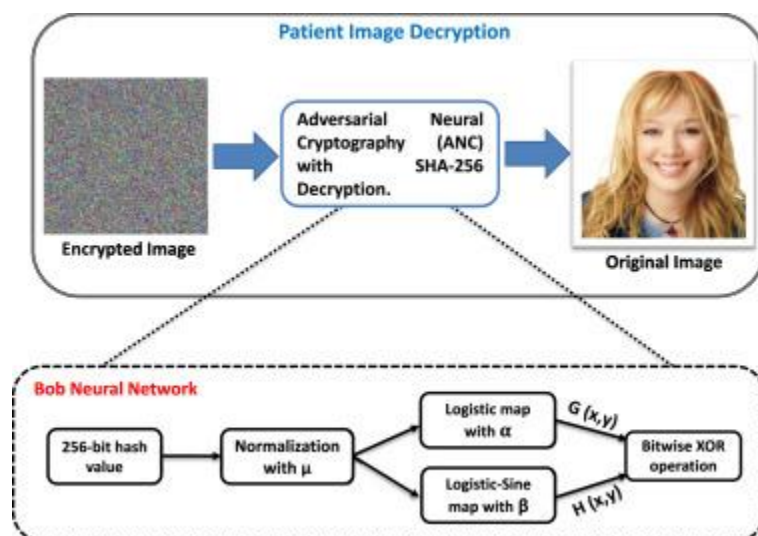


Fig. 3. The patient picture is decrypted using ANC and SHA-256.

#### 4. Region of non-interest RONI in medical images

As a result of the fact that a Region of Interest (ROI) in a medical picture is an essential region that is of diagnostic value, it is of the utmost importance to limit any changes that occur inside this region. It is necessary to use the greatest value of the cumulative gradient magnitude histogram to determine the gradient magnitude for each segment of the picture and successfully find the region of interest (ROI). The term "Region of Non-Interest" (RONI) refers to a block that is distinguished by an accumulated gradient magnitude value that is lower than the threshold parameter  $T$ , which has been specified. Given that it is less likely to have an impact on clinical judgments, this RONI component of the medical picture may integrate the EPR without affecting the integrity of the diagnostic process. When it comes to medical image processing, edge detection methods are often used to identify the region of interest (ROI) from the region of interest (RONI). As a consequence of this, RONIs generally display a lack of edge information or are located in regions of the picture that have smooth textures, as seen in Figure 4. The use of this method guarantees that the fundamental diagnostic characteristics are preserved in their original state while simultaneously enabling the safe incorporation of sensitive information into medical pictures.



Fig. 4. ROIs and RONIs of the Kidney medical image.

## 5. Proposed medical steganography technique

With the most promise for use in medical imaging, the LSB method is the most popular spatial domain methodology. There are better and more effective ways to hide payloads, but this one is easier to implement. This method assigns the specified values to the lower-left bits of the host image's chosen pixels. There is far less visual deterioration caused by LSB replacement (Go et al., 2013) due to the fact that changes to LSBs are not apparent to the HVS. The adaptive application of the suggested medical approach is made to the  $2 \times 2$ -pixel block. Two algorithms make it up: one for embedding and another for extracting the EPR, which includes information like the patient's name, date of birth, ID number, and doctor's name. By using the Histogram of Oriented Gradient (HOG) method to conceal EPR in medical pictures, the embedding algorithm selects a set of RONI using the LSB substitution approach. Either these areas fell into the smooth ones, or they included medical information with weak edges. Assuming that each RONI has a base pixel at the top-left that may contain locations chosen by RONIs, the LSB approach for embedding in each block is a great way to increase the embedding payload without sacrificing the visual quality or security of the DICOM picture. To conceal the secret bits, we use the other three pairs of neighboring pixels (EPR).

### 5.1. Histogram of oriented gradients (HOG)

The Histogram of Oriented Gradients (HOG) approach, which was presented by (Ye et al., 2021), is a powerful feature descriptor that is applied in computer vision and image processing, notably for object recognition. The HOG algorithm works in a manner that is similar to that of approaches such as the Canny Edge Detector and the Scale Invariant Feature Transform (SIFT). It does this by counting the number of instances of gradient orientations that occur inside certain sections of an image. Edge Orientation Histograms and SIFT are two methods that are comparable to this one; nonetheless, this approach is better than other edge descriptors since it places more emphasis on the structural elements of objects. For computing features, the HOG technique makes use of both the magnitude and angle of gradients, which contributes to the approach's increased efficiency. To be more specific, the method creates histograms for various parts of the picture by considering the amplitude and direction of the gradient. Following the derivation of the gradient magnitude from the x and y gradient images of the input medical picture, this value is then normalized such that it falls within the range of 0 to 1. The remaining phases of the technique for extracting and assembling HOG descriptors for all blocks throughout the detection window in a medical picture are shown in Figure 5. This figure also includes an illustration of the process. It is necessary to partition the detection window into tiny spatial sections, which are referred to as cells, in order to gather HOG descriptors successfully. These cells are where gradient information is calculated. After that, the histograms of each cell are generated based on the orientations of the gradients, and these histograms are then arranged into bigger blocks in order to offer a thorough representation of the characteristics of the object. By adhering to this systematic approach, the HOG algorithm is able to properly collect the information that is required for recognizing and analyzing items that are included inside medical pictures.



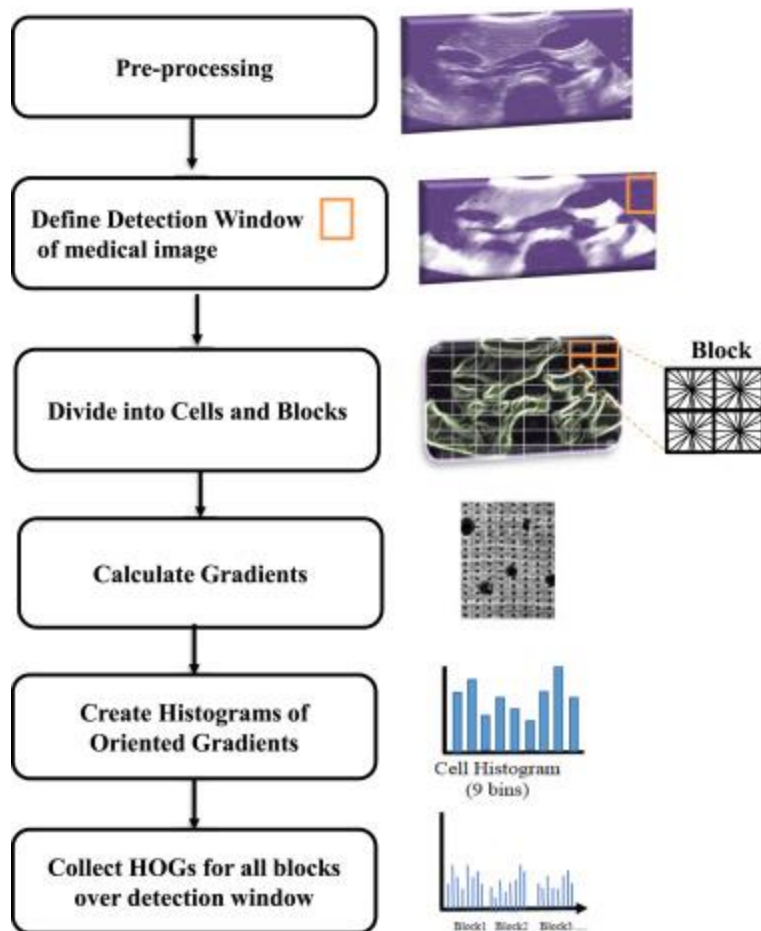


Fig. 5. An example of an oriented gradient histogram in a medical picture.

The approach that has been described includes a number of important pretreatment processes for the purpose of evaluating medical photographs. These procedures ensure that the data is properly prepared for further processing. Preprocessing is often necessary for medical pictures in order to improve features, eliminate noise, or normalize intensity values. The procedure of preprocessing might vary depending on the kind of image, such as magnetic resonance imaging (MRI), computed tomography (CT), or X-ray. This first step is essential for enhancing the quality of the picture and making it easier to conduct an accurate analysis. The next step is to establish the size and position of the detection window inside the medical picture. This window may contain the full image, or it may be confined to a Region of Interest (ROI) where the item of interest is anticipated to be identified. This helps to concentrate the analysis on regions that are pertinent to the investigation. After that, the detection window is segmented into smaller spatial sections that are referred to as cells. These cells are then joined together into bigger blocks, which enables the local contrast normalization that is necessary for managing fluctuations in light and shadowing. In the next step, the magnitude and direction of the gradient at each pixel inside the cells are calculated. This is a method that is sensitive to information on the texture and edges of the image, which permits the identification of relevant features. This histogram is used to capture the distribution of edge orientations in the picture. Last but not least, normalization is used to consider changes in illumination and contrast. This is of utmost significance in the field of medical imaging owing to the vast differences in lighting and contrast that exist across various imaging modalities and patient anatomy. By adhering to these procedures, the approach efficiently prepares medical pictures for

analysis, hence improving the identification and interpretation of essential aspects while preserving the integrity of the data that was initially collected.

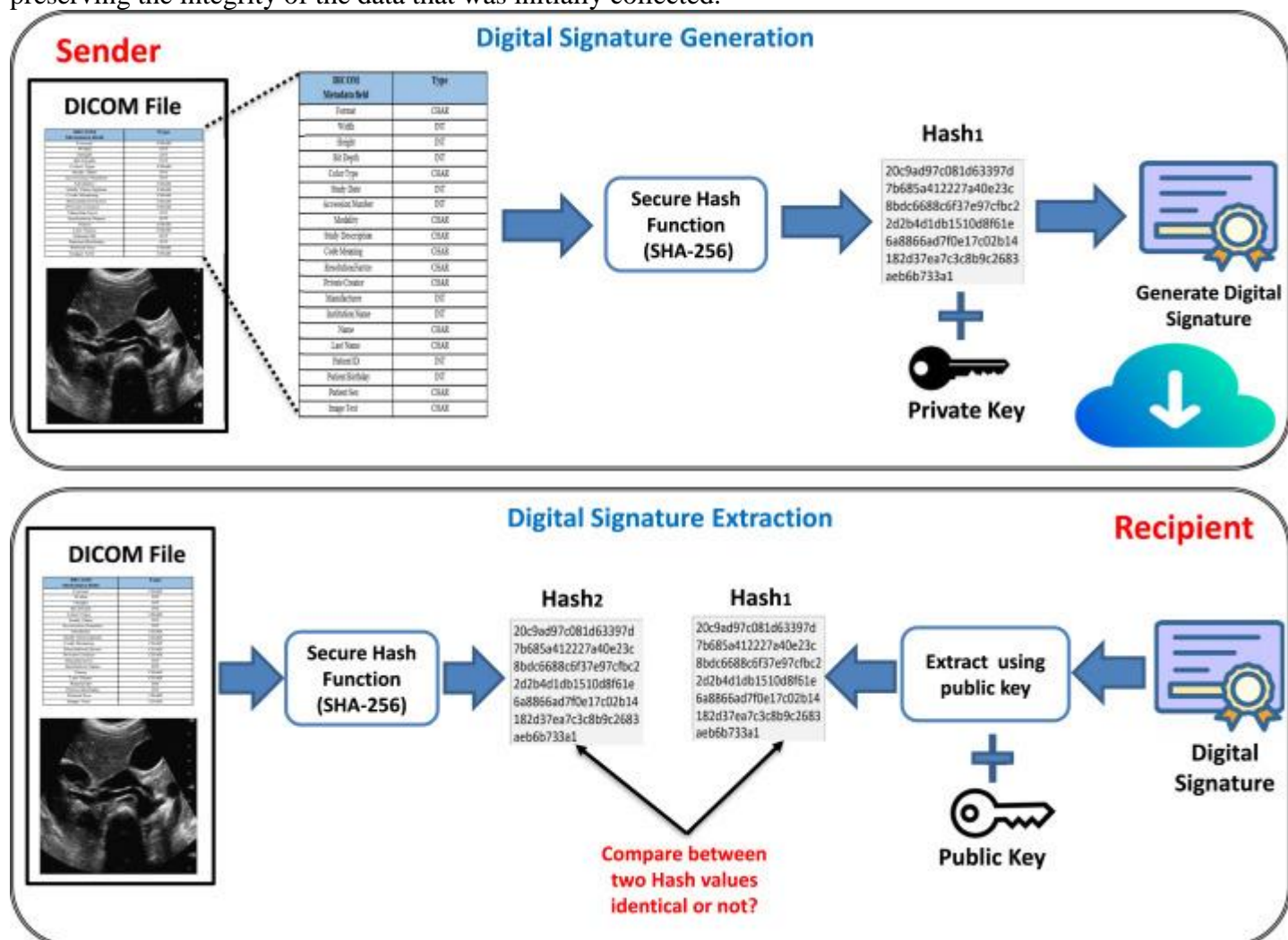


Fig. 6. SHA-256 is a safe hash method used for digital signature creation and extraction..

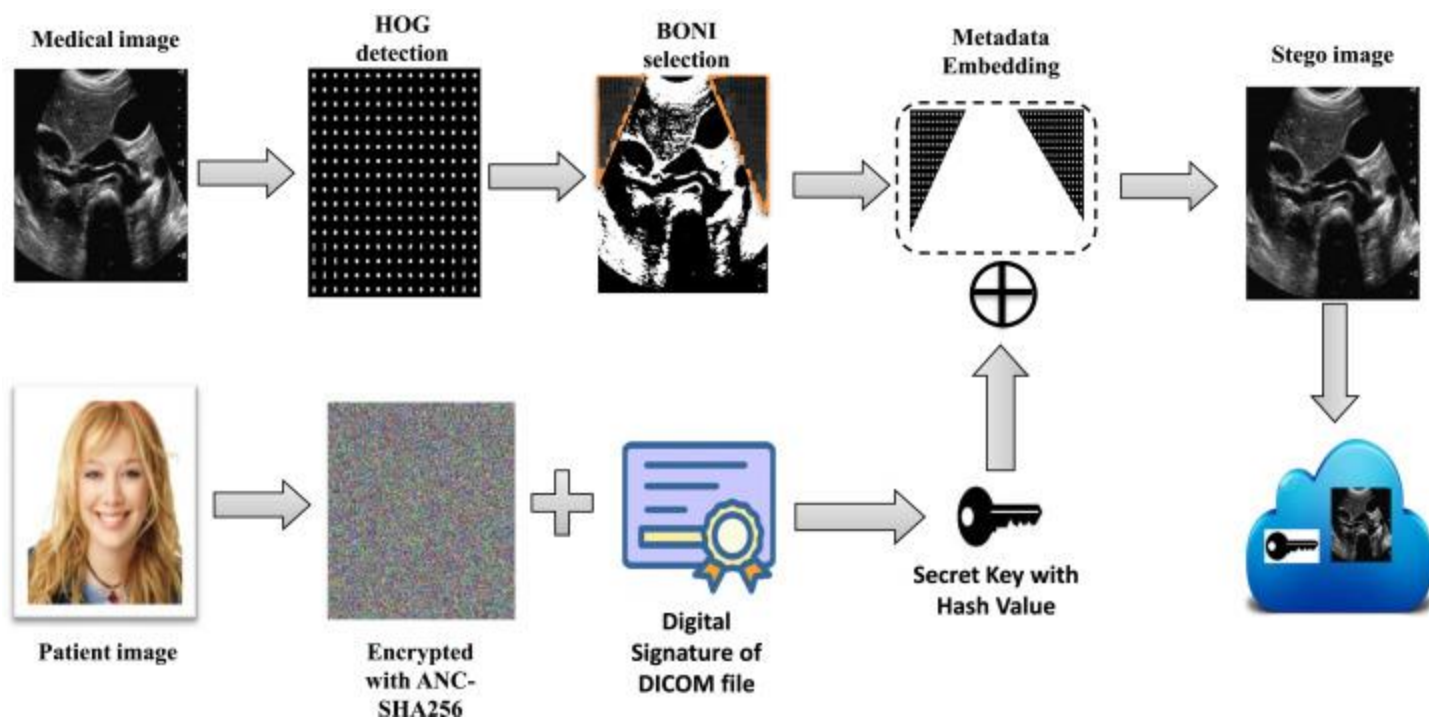


Fig. 7. Flow diagram for the process of integrating the DICOM file's digital signature and patient picture into a medical image.

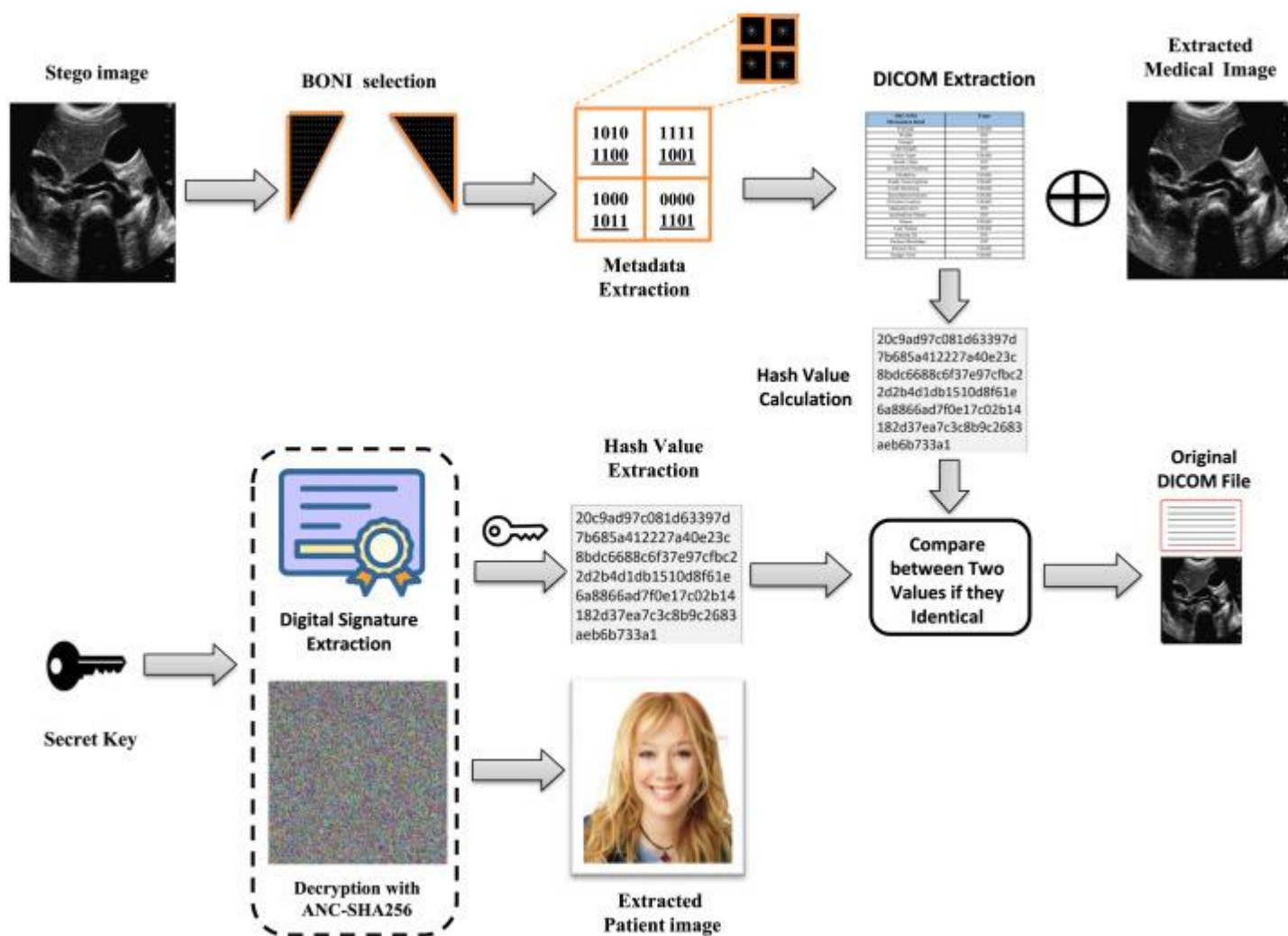


Fig. 8. Flow diagram for the extraction process used to get the original DICOM file and patient image.

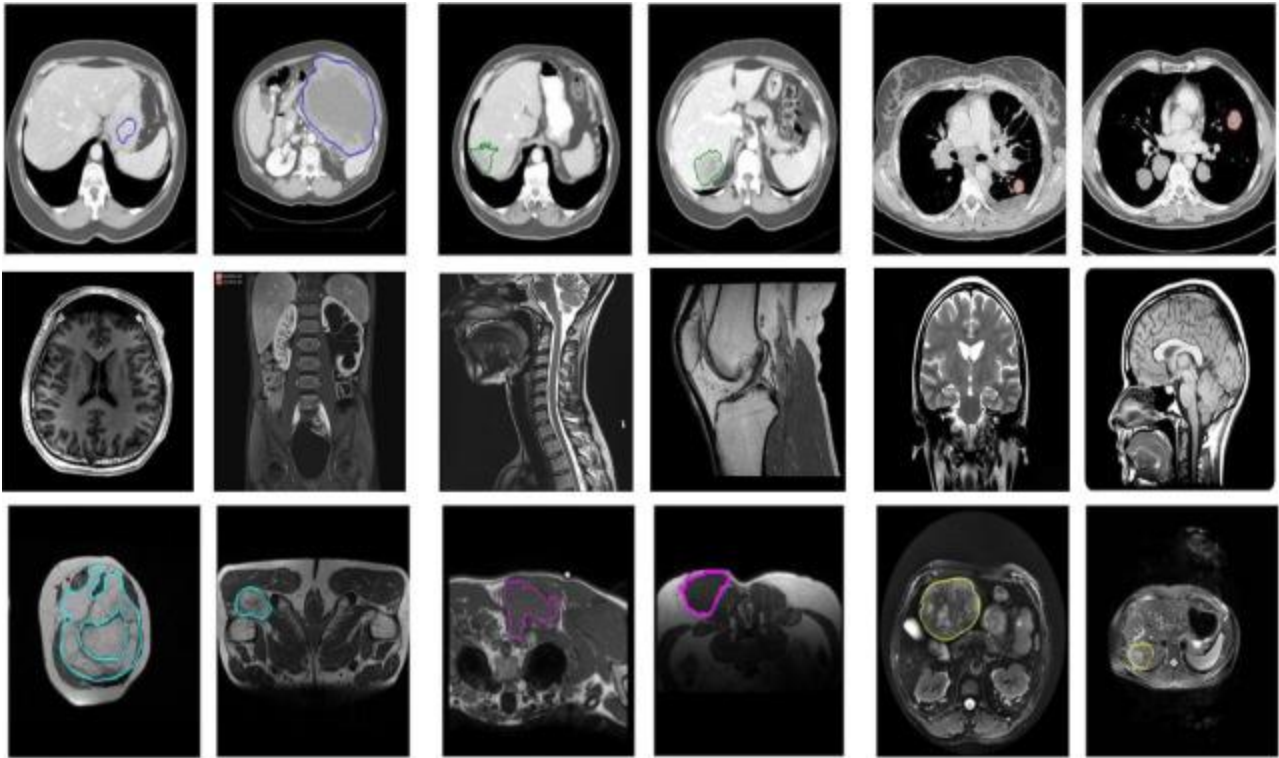


Fig. 9. Sample test images from MRI medical dataset.

### 5.2. Allocating digital signature

After being obtained, the DICOM file has to be reviewed to ensure that it has not been changed or modified in any way, as shown in Figure 6. For the purpose of ensuring that the contents of the DICOM file are accurate, it is recommended that the Secure Hash Algorithm (SHA-256) (Qian & Jiang, 2022) be used for the metadata that is included inside the file. This is done at the recipient. In the event that the outcomes of the comparison of the two hashes are equal, it is possible to conclude that the DICOM file that was transmitted and the one that was received by the receiver are identical. This would ensure that a third party did not alter the recovered file. In the event that a function comparison mismatch takes place, the file that has been received needs to be refused since this implies that the DICOM file has been altered for some reason.

### 5.3. Embedding procedure

In a DICOM file, the medical picture and the meta-data are kept distinct from one another. The encryption strategy for the patient's private picture is carried out using Adversarial Neural Cryptography with SHA-256 while the embedding operation is being carried out.

In conclusion, the information is hidden inside the medical picture, and the stego-image is produced in the manner shown in Figure 7. In this step, we typically set the threshold value to zero and the number of LSBs to one. This allows us to determine the true size of the chosen RONs for the purpose of concealing metadata. This includes the patient's secret picture as well as the digital signature. The following formula may be used to facilitate this process:

$$T_i = \lfloor \frac{t_{\min} + t_{\max}}{2} \rfloor \quad (3)$$

Although the  $T_i$  and  $K_i$  values are not suitable for the quantity of the metadata, we can adjust these values adaptively until all ROIs are accessible to conceal the DICOM file.



#### **5.4. Extraction procedure**

As shown in Figure 8, the second step of the HOG-LSB approach that has been presented includes the extraction phase. During this phase, the DICOM file and the concealed patient picture are extracted. Following the receipt of the stego medical picture by the receiver, the extraction procedure for the DICOM file and the patient's secret image will begin. The extraction approach is described by the phases that are listed below:

The first stage in the process is to determine the total number of pixels that belong to Regions of Interest (RONIs) by utilizing a base pixel, which is where the locations of the chosen RONIs are recorded. Extraction of the metadata from the DICOM file is accomplished by using the Least Significant Bit (LSB) extraction technique for each detected RONI. Following the successful extraction of the metadata from the stego-image, a hash value is computed using the SHA-256 method to guarantee the accurate representation of the data. At the same time, the ANC-SHA-256 decryption technique is used to obtain a picture of the particular patient. To validate the message's validity, the hash value calculated using the public key is compared to the hash value received. Last but not least, the DICOM file is recreated by including the extracted information together with the final medical picture. This ensures that the data that was collected is accurate and comprehensive. This methodical methodology guarantees that the concealed patient picture and the DICOM file connected with it are precisely recovered while preserving the integrity of the data that was initially collected.

#### **6. Experimental results and analysis**

This section presents the results of the experiments and the analysis that was performed in order to demonstrate the feasibility and effectiveness of the recommended HOG-LSB technique. In order to test and assess the model from the viewpoints of imperceptibility, capacity, and security, which are the major variables for picture steganography, all three of these aspects were considered. In addition, a number of datasets are used in order to evaluate the generalization capabilities of the HOG-LSB that has been presented.

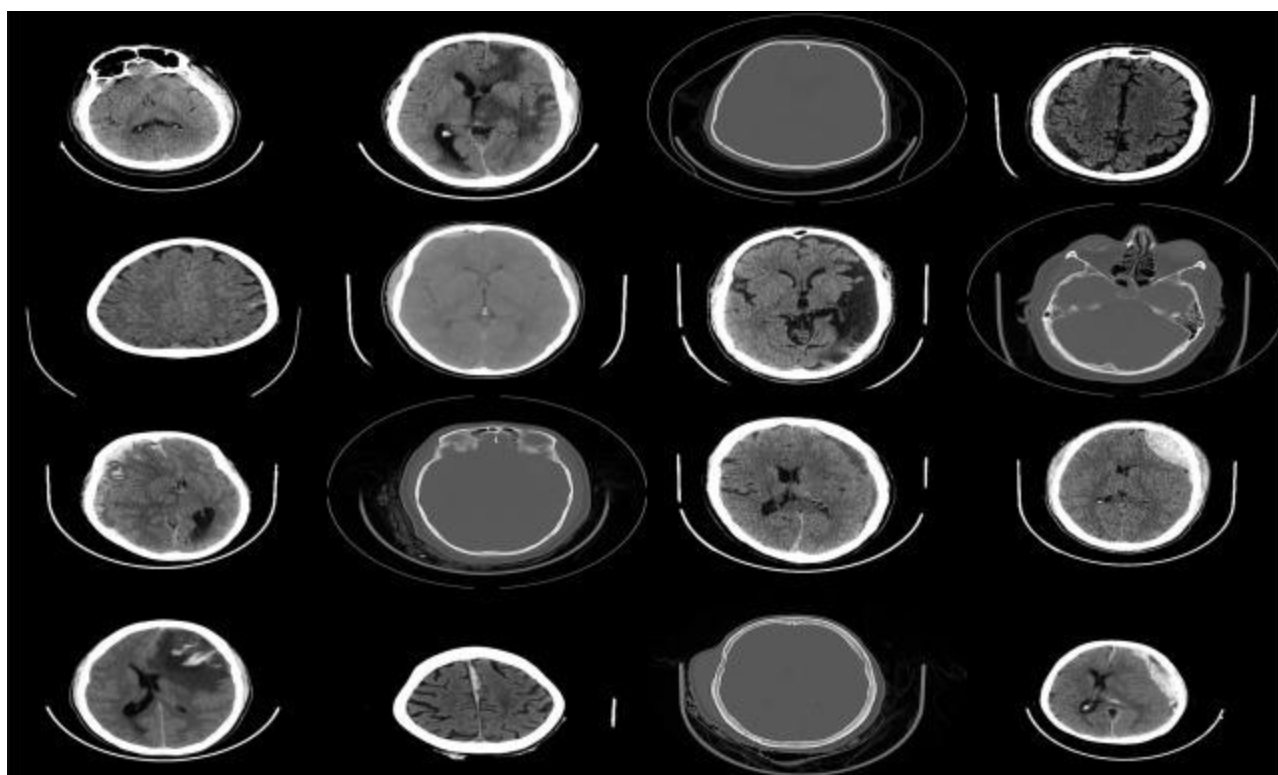


Fig. 10. Sample test pictures from a medical dataset of brain CT scans.



Fig. 11. Test picture samples from a medical X-ray dataset.

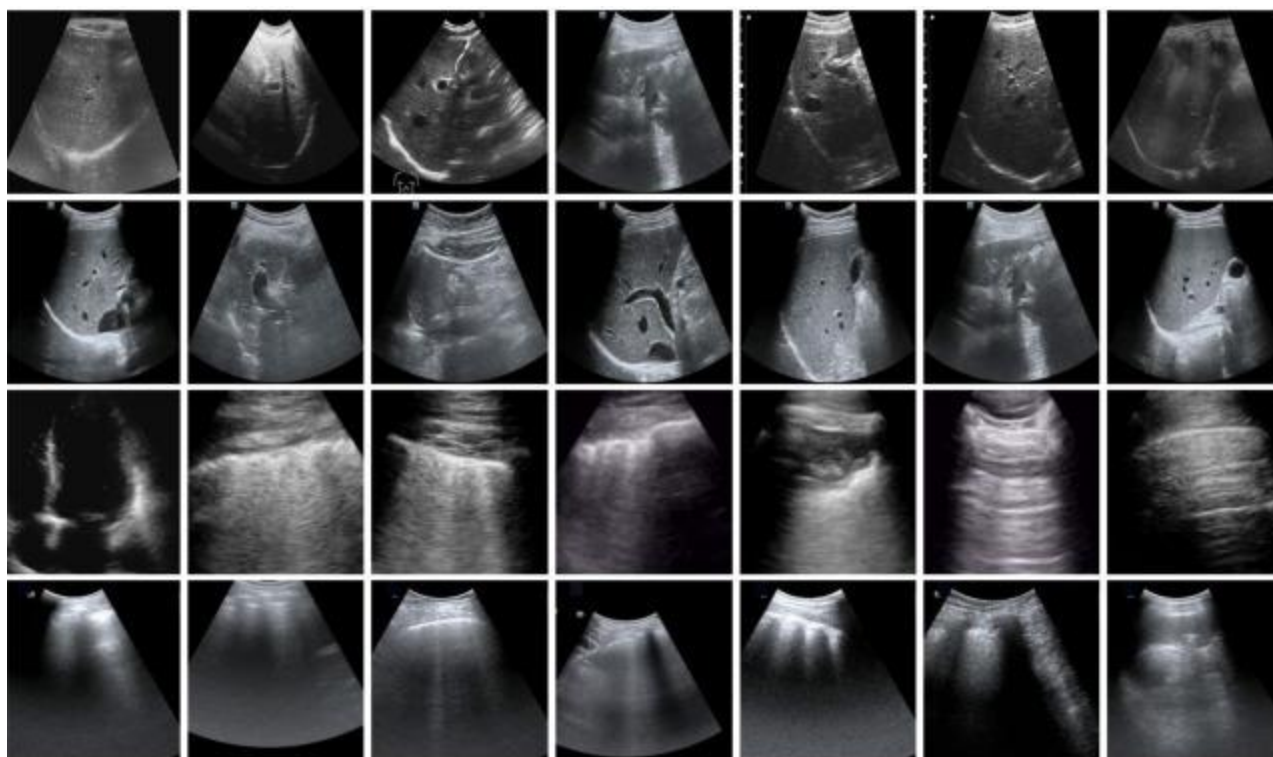


Fig. 12. Sample test photos from the medical ultrasound dataset.

### 6.1. Developmental environment and datasets

The following system specifications were used to perform the tests and analyze the results: MATLAB R2020b, an Intel® Core™ i7-7400 CPU running at 3.0 GHz, 16 GB of RAM, and Windows 10. Measurements of physical change, robustness, and visual quality were the main foci of the suggested technique's performance assessment. A total of four medical datasets were used to evaluate this approach. These datasets included a US Ultrasound dataset, an X-ray dataset, an MRI dataset, and a brain CT dataset. To guarantee a thorough evaluation, all pictures used in the trials were in DICOM format and did not undergo compression. The efficiency and effectiveness of our approach were assessed by randomly selecting a sample of RGB images sized  $56 \times 56$  from the LFW dataset (Alramadhan et al., 2017), as shown in Fig. 13, and subjecting it to rigorous testing using hundreds of medical images, as shown in Figs. 9, 10, 11, and 12. Reasons were given for using certain medical picture collections. The first major consideration is redundancy, which is common in medical imaging, especially in areas with consistent texture or intensity. In X-rays with big homogenous regions or, in particular, MRI sequences with predictable patterns, for example, this redundancy gives plenty of hiding places to insert secret data without affecting the original picture much. Also, characteristics that are unique to each modality are quite important. As an example, steganography may make good use of the natural noise levels in CT images. While maintaining the image's aesthetic quality, the suggested approach may modify certain noise patterns to include data. Moreover, dynamic sequences in ultrasound pictures allow steganography to sensitively manipulate pixel differences between frames without affecting diagnostic quality. Lastly, embedding capacity is a crucial factor to think about. We chose these datasets because they have enough redundancy to hide sensitive information without creating any noticeable artifacts. It is crucial to strike a balance between embedding capacity and the possible impact on picture



quality. Redundant datasets allow for better data hiding with a lower chance of discovery, making the steganographic approach more successful overall.



Fig. 13. Sample test images from LFW dataset.

## 6.2. Visual quality assessment

A subjective evaluation was carried out by steganalyst observers in order to evaluate the perceptual quality of stego-pictures, which are images that contain embedded secret data, and to guarantee that they closely match the original cover medical images. The stego media was analyzed to see whether or not there were any discernible differences between it and the cover media. In our evaluation, we focused on the following five essential metrics: Statistical measures such as Mean Square Error (MSE), Peak Signal-to-Noise Ratio (PSNR), Universal Quality Index (UQI), Structural Similarity Index Measure (SSIM), and Average Absolute Pixel Error (APE) are used in the analysis of image quality. The Mean Squared Error (MSE) is a metric that indicates the average squared difference in pixel values between the original picture and the stego-image. Lower MSE values suggest lesser discrepancies, which in turn indicates higher quality preservation. The peak signal-to-noise ratio (PSNR) is a measurement that is often used in combination with the mean squared error (MSE). It is a ratio that compares the greatest potential pixel value to the noise that is created by embedding. A greater PSNR indicates that there is a minimum perceived difference, which results in improved picture quality (Tang, 2022). In order to determine the statistical similarity between the cover and stego pictures, the UQI considers structural, brightness, and contrast features. Higher values indicate a greater degree of similarity between the two images (Bhargava et al., 2023). Similarly, SSIM measures perceptual quality by concentrating on structural information. This is necessary in order to ascertain whether or not the embedded picture maintains the structural integrity of the cover image. Last but not least, the average absolute difference in pixel values between the cover and stego-images is measured by the APE. Lower APE values suggest that there are minimum pixel changes and that there is a high level of visual quality preservation (Caicedo et al., 2021). In conjunction with one another, these metrics provide a strong and all-encompassing evaluation of the quality and perceptual integrity of the stego-image. This evaluation is critical for striking a balance between the payload capacity and the imperceptibility that is necessary for delicate medical applications.

$$\text{PSNR} = 10 \log_{10} \frac{(256-1)^2}{\text{MSE}} \quad (4)$$

$$\text{MSE} = \frac{1}{M \times N} \sum_{x=0}^{M-1} \sum_{y=0}^{N-1} (P_{x,y} - P'_{x,y})^2 \quad (5)$$

In this context, the dimensions (height and breadth) of the cover picture are represented by the symbol  $M \times N$ , which corresponds to the total number of pixels. This technique allows for the calculation of NCC values so we can evaluate the degree of similarity between the cover and stego pictures after embedding. This allows us to determine how well the concealed information can resist a variety of assaults without causing major distortion to the image. In addition, the Universal Quality Index (UQI) is applied as a statistical tool for the purpose of measuring the visual quality and levels of resemblance between the cover and stego or extracted photos. The structural fidelity and statistical correlation are both measured by UQI, which provides an understanding of the degree to which the stego picture is similar to the cover image that was created. It is a useful instrument for evaluating the quality of an image after embedding or extraction in steganographic procedures since it is computed by using a particular formula that was published by (Park et al., 2018). This formula takes into consideration elements such as brightness, contrast, and structure.

$$\text{UQI} = \frac{4\sigma_{xy}}{(\sigma_x^2 + \sigma_y^2)[(x)^2 + (y)^2]} \quad (6)$$

In addition, a visual quality metric known as UQI is examined in order to determine the degree of statistical resemblance that exists between the cover medial picture and the stego or extracted image. The following equation illustrates this to be the case:

$$\text{UQI} = \frac{4\sigma_{xy}}{(\sigma_x^2 + \sigma_y^2)[(x)^2 + (y)^2]} \quad (7)$$

$$\text{SSIM} = \frac{(2\mu_C\mu_S + c_1)(2\sigma_{CS} + c_2)}{(\mu_C^2 + \mu_S^2 + c_1)(\sigma_C^2 + \sigma_S^2 + c_2)} \quad (8)$$

$$\text{APE} = \frac{1}{M \times N} \sum_{i=0}^{M-1} \sum_{j=0}^{N-1} (x_{ij} - y_{ij}) \quad (9)$$

Using measures such as PSNR, SSIM, UQI, and APE, Table 1 displays the performance metrics of the proposed HOG-LSB steganographic approach. These metrics illustrate the usefulness of the method in embedding data inside different kinds of medical imaging, such as MRI, Brain-CT, X-ray, and ultrasound. Average values of 67.82 for PSNR, 0.9985 for SSIM, 0.9989 for UQI, and 3.75 for APE were reached by the approach when applied to MRI images. These numbers indicate that the method produced good quality with low noticeable distortion. When it comes to Brain-CT pictures, the findings further reinforce the notion that the embedded patient data is essentially undetectable. The approach produced an average PSNR of 69.89, an SSIM of 0.9989, a UQI of 0.9995, and an APE of 3.59. A similar pattern was seen with X-ray pictures, which demonstrated excellent efficiency with averages of 68.95 for PSNR, 0.9988 for SSIM, 0.9983 for UQI, and 3.67 for APE. Average values of 67.45 (PSNR), 0.9968 (SSIM), 0.9985 (UQI), and 3.98 (APE) were generated using ultrasound pictures, despite the fact that ultrasound images are normally more difficult to work with owing to their lower visual resolution. After embedding a patient picture measuring  $56 \times 56 \times 3$  and 6000 bits of information, these metrics together suggest that the approach successfully maintains high image quality across various datasets, making it free from visual artifacts. This is the case even after the patient image is embedded. The approach's resilience

and great fidelity in creating indistinguishable stego-images are confirmed by the overall average performance values for PSNR, SSIM, UQI, and APE across all datasets, which are respectively 68.53, 0.9983, 0.9988, and 3.75. This technology ensures that sensitive information may be safely incorporated without damaging the visual integrity required for medical analysis. It does this by selectively embedding data in Regions of Non-Interest (RONIs), which retains the diagnostic quality of medical pictures. A further evaluation of the performance of the proposed technique is shown in Table 2, which includes the evaluation of PSNR, SSIM, and UQI values for the extracted patient pictures. These values, which average 43.44, 0.9988, and 0.9983, respectively, are accompanied by APE values of 3.58, 3.74, and 3.51 across the Red, Green, and Blue channels accordingly. By demonstrating that the concealed patient data can be consistently recovered with no observable modification, these measures demonstrate that the original RGB quality of the embedded patient picture can be efficiently preserved. The fact that the suggested technology is able to safely and smoothly integrate medical data is shown by its high degree of imperceptibility and data fidelity. This makes it especially appropriate for applications in the field of telemedicine, where maintaining visual integrity is of utmost importance.

Table 1. Obtained results of the proposed HOG

– LSB technique in terms of PSNR, SSIM, UQI, and APE for stego and cover medical images.

| Image dataset     | Stego image vs. Cover image |              |             |                      |
|-------------------|-----------------------------|--------------|-------------|----------------------|
|                   | Average PSNR                | Average SSIM | Average UQI | Average APE of RONIs |
| <b>MRI</b>        | 67.82                       | 0.9985       | 0.9989      | 3.75                 |
| <b>Brain – CT</b> | 69.89                       | 0.9989       | 0.9995      | 3.59                 |
| <b>X – ray</b>    | 68.95                       | 0.9988       | 0.9983      | 3.67                 |
| <b>Ultrasound</b> | 67.45                       | 0.9968       | 0.9985      | 3.98                 |
| <b>Average</b>    | 68.53                       | 0.9983       | 0.9988      | 3.75                 |

Table 2. Obtained results of the proposed HOG

– LSB technique in terms of PSNR, SSIM, UQI, and APE for extracted and secret patient images.

| Image dataset     | Extracted image vs. Secret image |              |             |                     |
|-------------------|----------------------------------|--------------|-------------|---------------------|
|                   | Average PSNR                     | Average SSIM | Average UQI | Average APE R, G, B |
| <b>MRI</b>        | 42.93                            | 0.9998       | 0.9980      | 3.56, 3.85, 3.61    |
| <b>Brain – CT</b> | 44.09                            | 0.9989       | 0.9992      | 3.49, 3.52, 3.39    |
| <b>X – ray</b>    | 43.96                            | 0.9978       | 0.9984      | 3.52, 3.68, 3.46    |
| <b>Ultrasound</b> | 42.76                            | 0.9987       | 0.9974      | 3.74, 3.89, 3.56    |
| <b>Average</b>    | 43.44                            | 0.9988       | 0.9983      | 3.58, 3.74, 3.51    |

### 6.3. Protection against geometric attacks

The resilience of the suggested HOG-LSB steganographic approach against conventional geometric assaults such as rotation, scaling, and cropping is shown in Table 3. This method was

examined across six different picture categories: chest, eye, kidney, hand, foot, and brain. In order to evaluate the robustness of the concealed Electronic Patient Records (EPR) data contained inside each stego-image, these pictures, which were chosen from four different datasets, were subjected to diverse degrees of rotation, scaling, and cropping (Xu et al., 2018). The Normalized Cross-Correlation (NCC) metric was used for the assessment. This metric measures the degree of similarity that exists between the original cover picture and the processed stego image after secret bits have been implanted. The results of the NCC algorithm range from 0 to 1, with values closer to 1 indicating a greater degree of resemblance between the cover picture and the stego image. The NCC value of 1 represents total immunity to image processing assaults, which is a standard that our technology comes very close to achieving (N. D. Hunter, 2018). As seen in Table 3, the approach was able to acquire NCC values ranging from 0.9121 to 1 for rotational assaults, which are among the most prevalent types of geometric modifications. These values were reached for rotation angles of  $45^\circ$ ,  $90^\circ$ , and  $180^\circ$ . The fact that this range exists demonstrates that the suggested approach maintains a high level of resistance to rotation, which allows it to maintain the integrity of the embedded EPR data even after significant rotational rotations. The approach produced NCC values that ranged from 0.8726 to 1, proving once again that it is very resilient. These values were obtained from scaling experiments in which pictures were proportionately expanded or shrunk. This capability to survive scaling distortions is especially useful in the field of telemedicine, which often involves scaling images owing to the several available display formats. Last but not least, the approach was able to keep the NCC values over 0.9067 even after cropping, which is the process of removing areas of the picture that are located on the periphery. Cropping assaults, despite their significant impact, show a minimal effect on the detectability and retrieval of the embedded data, verifying the method's stability in the face of this form of change (Lewis & Campbell, 2017). When taken as a whole, these findings demonstrate that the HOG-LSB steganographic approach is very resistant to the geometric assaults that are most often used, hence maintaining both the integrity of the data and the quality of the picture. The technique's durability and usefulness for securely transferring medical data in real-world contexts, where similar image processing methods are often encountered, is shown by the fact that it maintains high NCC values while being subjected to a variety of modifications.



Fig. 14. Test picture samples chosen from six categories across four datasets..

Table 3. Obtained results of NCC values against different geometric attacks.

| Attacks  | Rate       | Brain  | Eye    | Kidney | Chest  | Hand   | Foot   |
|----------|------------|--------|--------|--------|--------|--------|--------|
| Rotation | $45^\circ$ | 0.9121 | 0.9321 | 0.9491 | 0.9321 | 0.9347 | 0.9144 |

| Attacks  | Rate | Brain  | Eye    | Kidney | Chest  | Hand   | Foot   |
|----------|------|--------|--------|--------|--------|--------|--------|
|          | 90°  | 0.9205 | 0.9589 | 0.9562 | 0.9769 | 0.9577 | 0.9562 |
|          | 180° | 1.000  | 1.000  | 1.000  | 0.9826 | 1.000  | 0.9988 |
| Scaling  | 0.5  | 0.9725 | 1.000  | 1.000  | 1.000  | 1.000  | 0.9987 |
|          | 1.5  | 0.9295 | 0.9671 | 0.9647 | 0.9769 | 0.9554 | 0.9672 |
|          | 2    | 0.8894 | 0.8826 | 0.8738 | 0.8726 | 0.8587 | 0.8921 |
| Cropping | 10%  | 0.9981 | 0.9999 | 0.9959 | 0.9893 | 0.9851 | 0.9860 |
|          | 20%  | 0.9647 | 0.9725 | 0.9628 | 0.9751 | 0.9532 | 0.9541 |
|          | 30%  | 0.9354 | 0.9204 | 0.9159 | 0.9067 | 0.9252 | 0.9174 |

#### 6.4. Protection against physical change

When embedding sensitive data such as medical information, it is essential to measure the physical change in cover media, such as photographs or audio files, in steganography. This is because the objective is to prevent any observable modifications that may potentially arouse suspicion (Hua et al., 2023). The change may be quantified with the use of many critical measures. The Peak Signal-to-Noise Ratio (PSNR) is one of the most often used metrics since it measures the difference between the original cover and the stego media after embedding. A greater PSNR indicates that there have been minimal alterations to the cover media. Greater PSNR values in the context of medical picture steganography are desired in order to guarantee that the cover image quality is preserved, which is necessary for conducting diagnostic procedures. An increase in the score of the Structural Resemblance Index (SSIM) indicates a greater resemblance between the original and stego media and, therefore, a more undetectable transformation. This index assesses the perceptual changes that occur between the two types of media. When it comes to medical applications, where the structural integrity of pictures must not be affected as much as possible, this parameter is essential. Additionally, the Universal Quality Index (UQI) provides additional assistance in the evaluation of quality by analyzing the degree of similarity that exists between the original picture and its stego equivalent. Higher UQI values indicate higher quality retention, which is essential in steganography, especially in telemedicine, where picture fidelity impacts both diagnosis and data privacy. Steganography is a field that is becoming more relevant. APE, on the other hand, evaluates the differences at the pixel level by determining the average absolute disparity between comparable pixels in the original and stego pictures. Lower APE values indicate a closer likeness between the two images. Both UQI and APE are essential for analyzing the effectiveness of steganographic algorithms. These metrics provide insights into the degree to which a method strikes a balance between concealment and quality retention. From the LFW dataset, six patient photos measuring 56×56 pixels were used to evaluate metadata sizes in four different ranges, which are shown in Table 4 of the proposed HOG-LSB approach. These ranges include 2000–3000 bits, 3000–4000 bits, 4000–5000 bits, and 5000–6000 bits. A strong concealment with excellent visual quality that is practically unnoticeable to the Human Visual System (HVS) is shown by the results of the proposed approach, which exhibit a high average PSNR of 67.55 dB. A number of other important metrics, including NCC, SSIM, UQI, and APE, displayed an average value of 0.9959, 0.9887, 0.9859, and 3.83, respectively. This highlights the fact that there are only minor differences between the cover and stego-images. These findings

provide evidence that the approach can include a substantial payload, which encompasses patient photos of  $56 \times 56 \times 3$  and 6000 metadata bits, while simultaneously preserving exceptional image quality and being undetectable. Therefore, the HOG-LSB approach that was presented exhibits an excellent balance between the ability to embed data and the imperceptibility of the data, which makes it extremely ideal for applications that need safe but transparent medical data transfer.

Table 4. Obtained results of PSNR, NCC, SSIM, UQI, and APE of the proposed technique HOG – LSB at different metadata sizes of bits.

| Medical Image | Patient Image (bits)    | Metadata Size (bits) | PSNR (dB) | NCC    | SSIM   | UQI    | APE  |
|---------------|-------------------------|----------------------|-----------|--------|--------|--------|------|
| Brain         | $56 \times 56 \times 3$ | 2000–3000            | 69.82     | 0.9988 | 0.9899 | 0.9799 | 3.25 |
|               |                         | 3000–4000            | 69.37     | 0.9986 | 0.9896 | 0.9789 | 3.54 |
|               |                         | 4000–5000            | 68.92     | 0.9980 | 0.9893 | 0.9779 | 3.83 |
|               |                         | 5000–6000            | 68.47     | 0.9960 | 0.9890 | 0.9769 | 4.12 |
| Eye           | $56 \times 56 \times 3$ | 2000–3000            | 69.87     | 0.9978 | 0.9898 | 0.9798 | 3.44 |
|               |                         | 3000–4000            | 69.22     | 0.9948 | 0.9885 | 0.9888 | 3.65 |
|               |                         | 4000–5000            | 68.57     | 0.9918 | 0.9882 | 0.9887 | 3.86 |
|               |                         | 5000–6000            | 67.92     | 0.9915 | 0.9879 | 0.9868 | 4.07 |
| Kidney        | $56 \times 56 \times 3$ | 2000–3000            | 65.49     | 0.9989 | 0.9875 | 0.9869 | 3.51 |
|               |                         | 3000–4000            | 65.04     | 0.9974 | 0.9881 | 0.9853 | 3.77 |
|               |                         | 4000–5000            | 64.59     | 0.9952 | 0.9877 | 0.9831 | 4.03 |
|               |                         | 5000–6000            | 64.14     | 0.9950 | 0.9873 | 0.9809 | 4.29 |
| Chest         | $56 \times 56 \times 3$ | 2000–3000            | 66.27     | 0.9981 | 0.9878 | 0.9868 | 3.68 |
|               |                         | 3000–4000            | 65.62     | 0.9951 | 0.9878 | 0.9876 | 3.95 |
|               |                         | 4000–5000            | 64.97     | 0.9921 | 0.9874 | 0.9874 | 4.22 |
|               |                         | 5000–6000            | 64.32     | 0.9891 | 0.9860 | 0.9872 | 4.49 |
| Foot          | $56 \times 56 \times 3$ | 2000–3000            | 69.49     | 0.9977 | 0.9889 | 0.9889 | 3.44 |
|               |                         | 3000–4000            | 69.04     | 0.9975 | 0.9896 | 0.9887 | 3.69 |
|               |                         | 4000–5000            | 68.59     | 0.9971 | 0.9893 | 0.9885 | 3.94 |
|               |                         | 5000–6000            | 68.14     | 0.9967 | 0.9890 | 0.9883 | 4.19 |
| Hand          | $56 \times 56 \times 3$ | 2000–3000            | 68.72     | 0.9978 | 0.9898 | 0.9788 | 3.14 |
|               |                         | 3000–4000            | 68.47     | 0.9975 | 0.9896 | 0.9887 | 3.55 |
|               |                         | 4000–5000            | 68.22     | 0.9952 | 0.9893 | 0.9876 | 3.96 |
|               |                         | 5000–6000            | 67.97     | 0.9929 | 0.9890 | 0.9865 | 4.37 |



| Medical Image | Patient Image (bits) | Metadata Size (bits) | PSNR (dB) | NCC    | SSIM   | UQI    | APE  |
|---------------|----------------------|----------------------|-----------|--------|--------|--------|------|
| Average       |                      |                      | 67.55     | 0.9959 | 0.9887 | 0.9859 | 3.83 |

### 6.5. Protection against histogram analysis

After embedding, the histogram assessment is mostly carried out with the purpose of locating and evaluating any hidden data relics that may have been caused in the cover picture. It is easy to compute the amount of the secret message, particularly when embedding has been extremely high. This indicates that steg analysts are able to identify any modifications with ease by using HVS (Hameed et al., 2019). As a consequence of this, we are able to carry out this histogram assessment in accordance with the way that was suggested between cover and stego pictures for the medical images that were discussed previously in Figure 14. In Figure 15, Figure 16, Figure 17, Figure 18, Figure 19, and Figure 20, six medical photos have been examined. These images involve the eye, the chest, the brain, the hand, the foot, and the kidney. Additionally, histograms of cover images and their related stego images have been included. These images were created using the HOG-LSB approach. Stego-images, on the other hand, have higher imperceptibility and security, as shown by the fact that there is no fluctuation between the histograms. Because of this, the embedding process is better in its capacity to conceal color pictures and digital signatures without being discovered by histogram assessment.

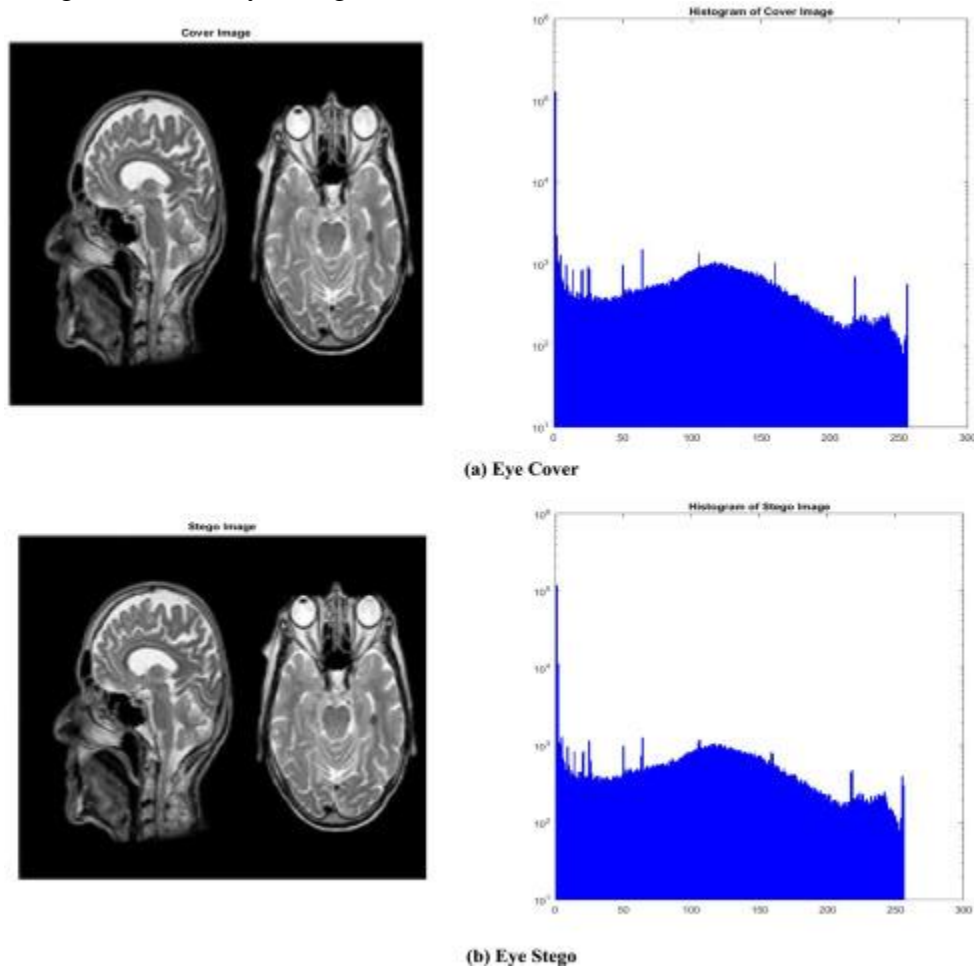


Fig. 15. Histogram analysis of the Eye cover and its stego-image using the suggested HOG-LSB approach.

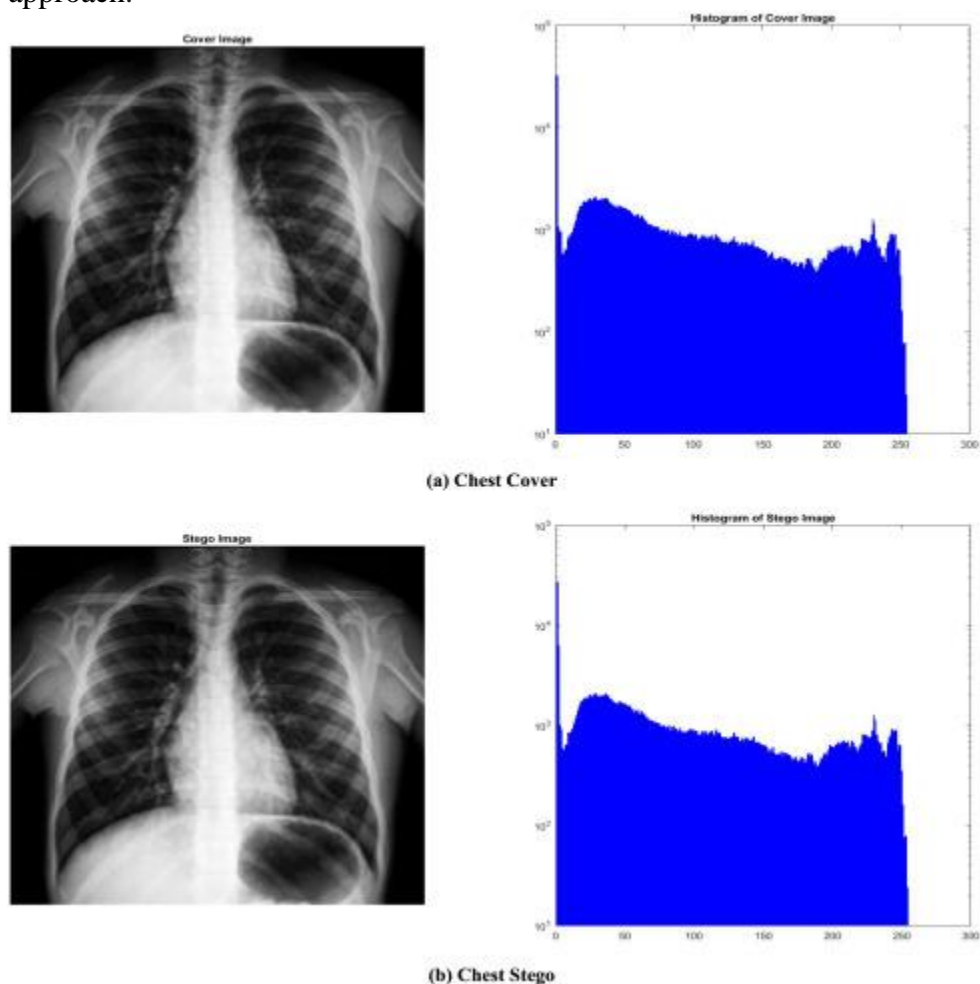


Fig. 16. Histogram analysis of the chest cover and its stego-image using the suggested HOG-LSB approach.



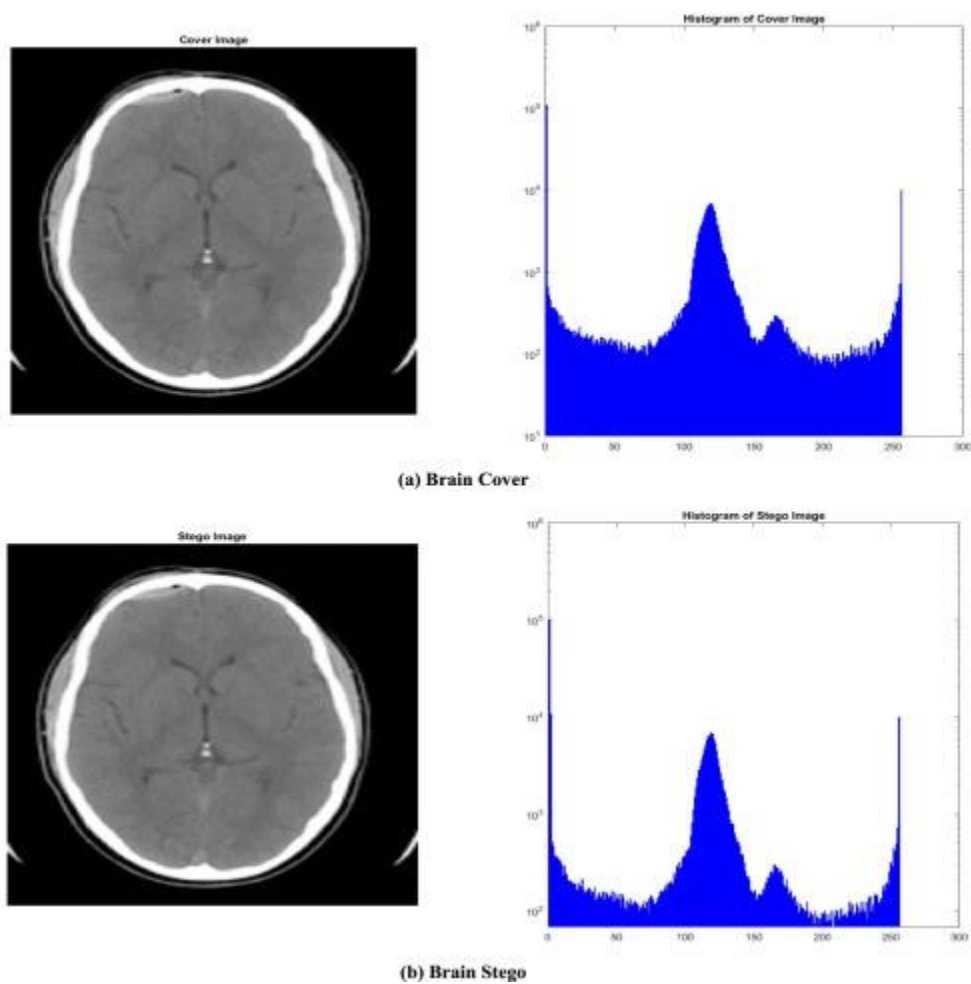


Fig. 17. Histogram analysis of the Brain cover and its stego picture using the suggested HOG-LSB approach.

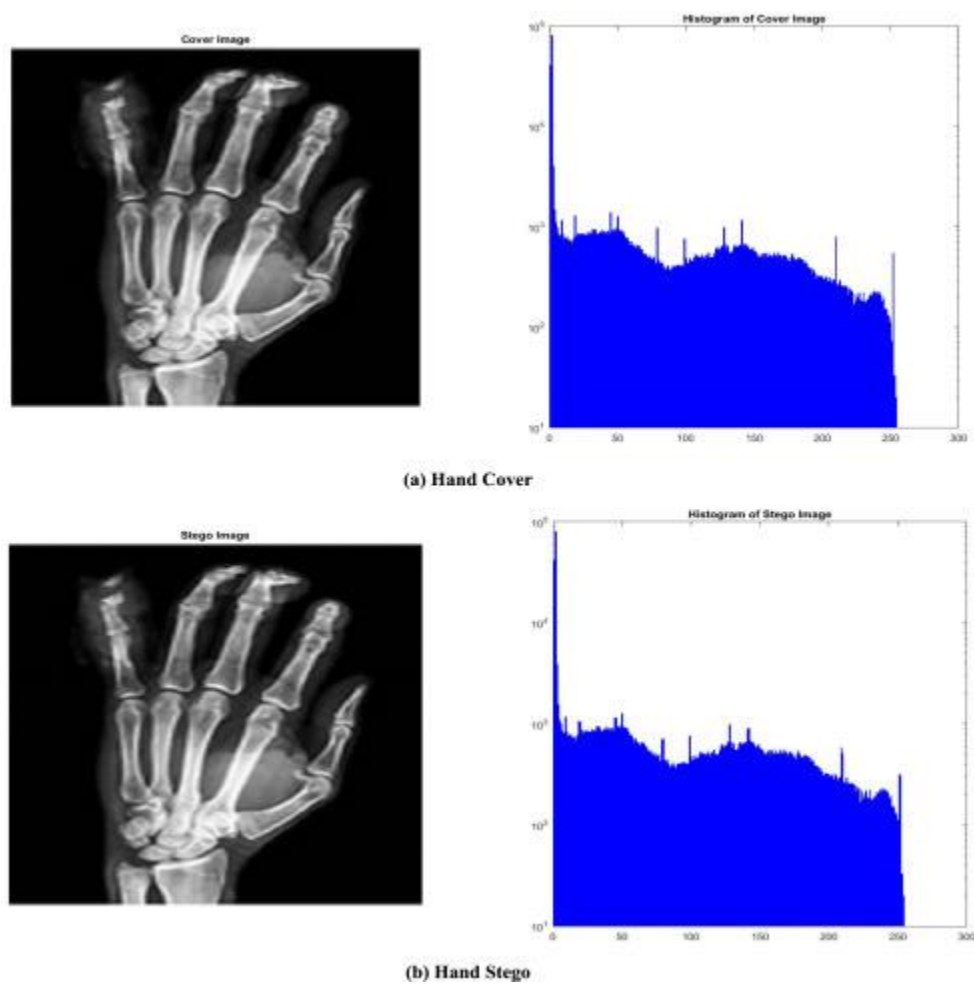


Fig. 18. Histogram analysis of the Hand cover and its stego-image using the suggested HOG-LSB approach.

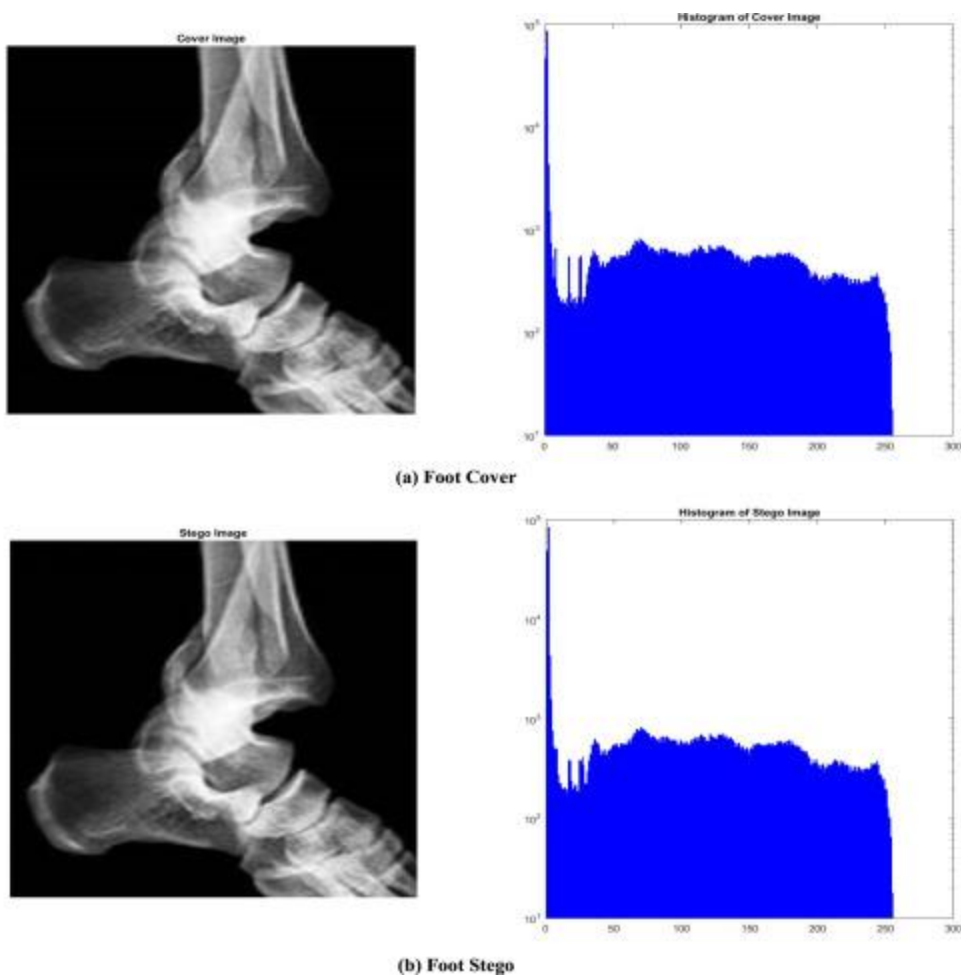


Fig. 19. Histogram analysis of the Foot cover and its stego-image using the suggested HOG-LSB approach.

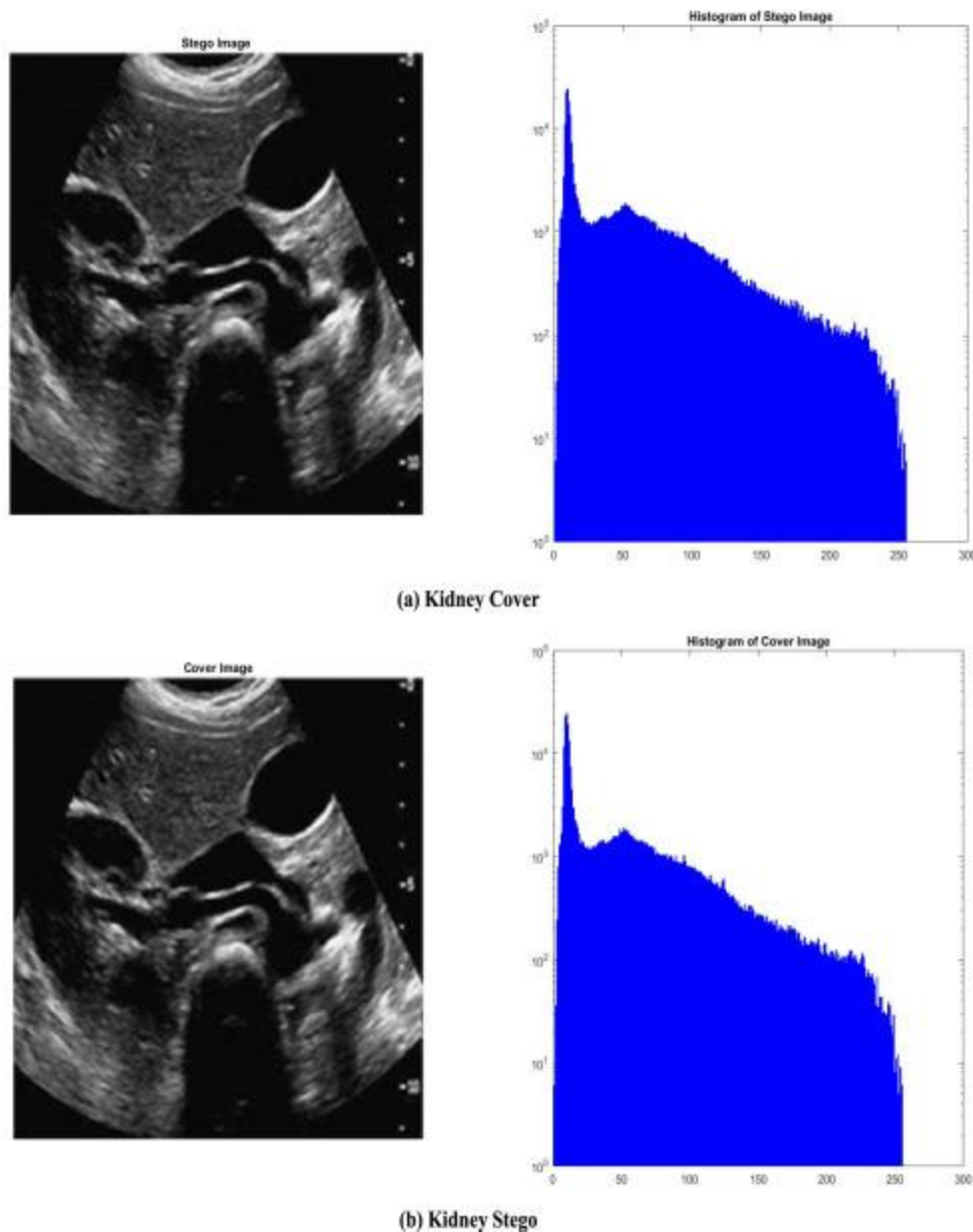


Fig. 20. Histogram analysis of the kidney cover and its stego-image using the suggested HOG-LSB approach.

### 6.6. Comparative analysis with existing hiding techniques

The comparison of the proposed HOG-LSB data-hiding strategy with prior state-of-the-art techniques illustrates its efficacy in preserving high visual quality, resilience, and imperceptibility across diverse metadata sizes and categories of medical images. The suggested approach consistently attains elevated Peak Signal-to-Noise Ratio (PSNR) values, low Mean Squared Error (MSE), and outstanding Structural Similarity Index (SSIM) scores, even with higher metadata volumes. For example, regarding brain images, the HOG-LSB method achieves a PSNR of 76.79 dB, an MSE of 0, and an SSIM of 1.000 for metadata sizes ranging from 650 to 950 bits, surpassing the recent methodologies by (Van Hout et al., 2023), which report PSNRs of 69.82 dB and 72.36 dB, respectively, accompanied by elevated MSE and marginally reduced SSIM values. The pattern

|      | <b>Im Metadata size</b><br>(bits) | {Formatting Citation} |            |             | (Chen et al., 2011) |            |             | (Besharov et al., 2013) |            |             |
|------|-----------------------------------|-----------------------|------------|-------------|---------------------|------------|-------------|-------------------------|------------|-------------|
|      |                                   | <b>PSNR (dB)</b>      | <b>MSE</b> | <b>SSIM</b> | <b>PSNR (dB)</b>    | <b>MSE</b> | <b>SSIM</b> | <b>PSNR (dB)</b>        | <b>MSE</b> | <b>SSIM</b> |
| Bra  | 650–950                           | 74.36                 | 0          | 0.9844      | 75.55               | 0.01       | 0.9988      | 75.84                   | 0.005      | 0.9998      |
|      | 950–1250                          | 73.22                 | 0          | 0.9832      | 73.47               | 0.01       | 0.9988      | 73.67                   | 0.005      | 0.9997      |
|      | 1250–1550                         | 72.14                 | 0          | 0.9712      | 72.21               | 0.01       | 0.9988      | 72.61                   | 0.005      | 0.9996      |
|      | 1550–1850                         | 71.58                 | 0          | 0.9614      | 71.68               | 0.01       | 0.9888      | 71.74                   | 0.005      | 0.9995      |
| Eye  | 650–950                           | 68.65                 | 0.01       | 0.9862      | 69.41               | 0.01       | 0.9885      | 69.76                   | 0.005      | 0.9997      |
|      | 950–1250                          | 67.21                 | 0.01       | 0.9744      | 68.65               | 0.01       | 0.9888      | 69.35                   | 0.005      | 0.9996      |
|      | 1250–1550                         | 66.17                 | 0.02       | 0.9957      | 67.59               | 0.01       | 0.9888      | 68.57                   | 0.005      | 0.9994      |
|      | 1550–1850                         | 65.53                 | 0.02       | 0.9882      | 66.87               | 0.01       | 0.9888      | 67.37                   | 0.005      | 0.9992      |
| Kid  | 650–950                           | 68.32                 | 0.01       | 0.9896      | 68.35               | 0.01       | 0.9888      | 68.35                   | 0.005      | 0.9998      |
|      | 950–1250                          | 67.08                 | 0.01       | 0.9832      | 66.47               | 0.01       | 0.9888      | 66.47                   | 0.005      | 0.9997      |
|      | 1250–1550                         | 66.07                 | 0.02       | 0.9832      | 66.18               | 0.01       | 0.9888      | 66.18                   | 0.005      | 0.9996      |
|      | 1550–1850                         | 65.57                 | 0.02       | 0.9832      | 66.04               | 0.01       | 0.9888      | 66.04                   | 0.005      | 0.9995      |
| Che  | 650–950                           | 72.84                 | 0.01       | 0.9832      | 72.56               | 0.01       | 0.9888      | 72.56                   | 0.005      | 0.9995      |
|      | 950–1250                          | 71.24                 | 0.01       | 0.9832      | 71.39               | 0.01       | 0.9888      | 71.39                   | 0.005      | 0.9994      |
|      | 1250–1550                         | 69.84                 | 0.02       | 0.9832      | 69.89               | 0.01       | 0.9888      | 69.89                   | 0.005      | 0.9993      |
|      | 1550–1850                         | 68.14                 | 0.02       | 0.9832      | 68.44               | 0.01       | 0.9854      | 68.44                   | 0.005      | 0.9992      |
| Foot | 650–950                           | 72.84                 | 0.01       | 0.9832      | 72.56               | 0.01       | 0.9888      | 72.56                   | 0.005      | 0.9995      |
|      | 950–1250                          | 71.24                 | 0.01       | 0.9832      | 71.39               | 0.01       | 0.9888      | 71.39                   | 0.005      | 0.9994      |
|      | 1250–1550                         | 69.84                 | 0.02       | 0.9832      | 69.89               | 0.01       | 0.9888      | 69.89                   | 0.005      | 0.9993      |
|      | 1550–1850                         | 68.14                 | 0.02       | 0.9832      | 68.44               | 0.01       | 0.9854      | 68.44                   | 0.005      | 0.9992      |
| Hand | 650–950                           | 68.65                 | 0.01       | 0.9862      | 69.41               | 0.01       | 0.9885      | 69.76                   | 0.005      | 0.9997      |
|      | 950–1250                          | 67.21                 | 0.01       | 0.9744      | 68.65               | 0.01       | 0.9888      | 69.35                   | 0.005      | 0.9996      |
|      | 1250–1550                         | 66.17                 | 0.02       | 0.9957      | 67.59               | 0.01       | 0.9888      | 68.57                   | 0.005      | 0.9994      |
|      | 1550–1850                         | 65.53                 | 0.02       | 0.9882      | 66.87               | 0.01       | 0.9888      | 67.37                   | 0.005      | 0.9992      |

persists across various metadata sizes, with the suggested method demonstrating uniform quality and little perceived effects on picture fidelity. In eye pictures, the suggested approach maintains a high PSNR of 76.57 dB for lower metadata sizes (650–950 bits) and experiences a mild decline with bigger metadata, indicating a predictable slight effect on visual quality due to greater data embedding. In comparison to the methodologies used, which provide PSNR values of around 69.87 dB and 69.95 dB, respectively, the HOG-LSB technique demonstrates superiority, reflecting a more favorable equilibrium between picture quality and data hiding. This tendency is also observable in other picture categories, such as kidney, chest, and hand images, where the HOG-LSB technique maintains elevated SSIM values approaching 1.000, demonstrating no perceptual distortion and signifying that the concealed data stays undetectable to human perception. The

| Image      | Metadata size<br>(bits) | (Hashmi et al., 2021) |       |        | (Chen et al., 2011) |      |        | Proposed HOG<br>– LSB Technique |       |        |
|------------|-------------------------|-----------------------|-------|--------|---------------------|------|--------|---------------------------------|-------|--------|
|            |                         | PSNR (dB)             | MSE   | SSIM   | PSNR (dB)           | MSE  | SSIM   | PSNR (dB)                       | MSE   | SSIM   |
| Empty Cell | 650–950                 | 69.82                 | 0     | 0.9899 | 72.36               | 0.01 | 0.9877 | 76.79                           | 0     | 1.000  |
|            | 950–1250                | 69.37                 | 0     | 0.9896 | 71.22               | 0.02 | 0.9865 | 74.03                           | 0     | 1.000  |
|            | 1250–1550               | 68.92                 | 0     | 0.9893 | 70.08               | 0.02 | 0.9853 | 73.29                           | 0     | 1.000  |
|            | 1550–1850               | 68.47                 | 0     | 0.989  | 68.94               | 0.03 | 0.9841 | 71.82                           | 0     | 1.000  |
| Brain      | 650–950                 | 69.87                 | 0.002 | 0.9888 | 69.95               | 0.01 | 0.9885 | 76.57                           | 0.001 | 0.9999 |
|            | 950–1250                | 69.22                 | 0.003 | 0.9885 | 69.21               | 0.03 | 0.9848 | 74.74                           | 0.002 | 0.9999 |
|            | 1250–1550               | 68.57                 | 0.004 | 0.9882 | 68.47               | 0.05 | 0.9811 | 73.75                           | 0.003 | 0.9998 |
|            | 1550–1850               | 67.52                 | 0.005 | 0.9879 | 67.73               | 0.07 | 0.9774 | 72.75                           | 0.004 | 0.9999 |
| Eye        | 650–950                 | 65.49                 | 0.002 | 0.9885 | 68.32               | 0.02 | 0.9877 | 68.39                           | 0.001 | 0.9997 |
|            | 950–1250                | 65.04                 | 0.003 | 0.9881 | 67.08               | 0.03 | 0.9865 | 67.94                           | 0.002 | 0.9999 |
|            | 1250–1550               | 64.59                 | 0.004 | 0.9877 | 66.07               | 0.04 | 0.9853 | 66.96                           | 0.003 | 0.9998 |
|            | 1550–1850               | 64.14                 | 0.005 | 0.9873 | 65.57               | 0.05 | 0.9841 | 66.63                           | 0.004 | 0.9997 |
| Kidney     | 650–950                 | 66.27                 | 0.002 | 0.9882 | 72.84               | 0.02 | 0.9765 | 75.88                           | 0.001 | 0.9999 |
|            | 950–1250                | 65.62                 | 0.004 | 0.9878 | 71.24               | 0.03 | 0.9748 | 71.85                           | 0.002 | 0.9999 |
|            | 1250–1550               | 64.97                 | 0.006 | 0.9874 | 69.84               | 0.04 | 0.9731 | 69.95                           | 0.003 | 0.9998 |
|            | 1550–1850               | 64.32                 | 0.008 | 0.9866 | 68.14               | 0.05 | 0.9714 | 68.93                           | 0.004 | 0.9997 |
| Chest      | 650–950                 | 69.49                 | 0.003 | 0.9899 | 72.84               | 0.01 | 0.9877 | 75.88                           | 0.001 | 0.9999 |
|            | 950–1250                | 69.04                 | 0.005 | 0.9896 | 71.24               | 0.01 | 0.9865 | 71.85                           | 0.002 | 0.9999 |
|            | 1250–1550               | 68.59                 | 0.007 | 0.9893 | 69.84               | 0.03 | 0.9853 | 69.95                           | 0.003 | 0.9998 |
|            | 1550–1850               | 68.14                 | 0.009 | 0.9897 | 68.44               | 0.03 | 0.9841 | 68.93                           | 0.004 | 0.9997 |
| Foot       | 650–950                 | 68.72                 | 0.002 | 0.9899 | 68.75               | 0.02 | 0.9765 | 76.57                           | 0.001 | 0.9999 |
|            | 950–1250                | 68.47                 | 0.004 | 0.9896 | 67.21               | 0.03 | 0.9748 | 74.74                           | 0.002 | 0.9999 |
|            | 1250–1550               | 67.22                 | 0.006 | 0.9893 | 67.47               | 0.03 | 0.9731 | 73.75                           | 0.003 | 0.9998 |
|            | 1550–1850               | 67.57                 | 0.008 | 0.9895 | 67.63               | 0.04 | 0.9754 | 72.75                           | 0.004 | 0.9999 |
| Hand       | 650–950                 | 68.72                 | 0.002 | 0.9899 | 68.75               | 0.02 | 0.9765 | 76.57                           | 0.001 | 0.9999 |
|            | 950–1250                | 68.47                 | 0.004 | 0.9896 | 67.21               | 0.03 | 0.9748 | 74.74                           | 0.002 | 0.9999 |
|            | 1250–1550               | 67.22                 | 0.006 | 0.9893 | 67.47               | 0.03 | 0.9731 | 73.75                           | 0.003 | 0.9998 |
|            | 1550–1850               | 67.57                 | 0.008 | 0.9895 | 67.63               | 0.04 | 0.9754 | 72.75                           | 0.004 | 0.9999 |

resilience of the HOG-LSB approach against geometric and statistical assaults, seen by the low MSE values, underscores its suitability for sensitive applications, especially in telemedicine. The elevated PSNR values attained by the proposed technique across diverse metadata sizes and medical picture categories indicate its superior ability to safely obscure EPR data while preserving the high-quality visuals crucial for medical imaging analysis. The methodology surpasses conventional techniques by routinely attaining near-perfect SSIM values, indicating a significant level of structural similarity between the original and stego pictures. The proposed HOG-LSB technique surpasses the benchmarks established by prior methods, providing an efficient solution that guarantees both security and image quality, thereby facilitating the secure transmission of medical information over networks without sacrificing visual fidelity.

Table 5. Comparison of the proposed technique with the state – of – the  
– art data hiding techniques in terms of various metadata sizes.

Table 6. Comparison of the proposed technique with the state – of – the  
– art data hiding techniques in terms of various metadata sizes.

## 7. Conclusion

This work introduces a sophisticated data-hiding method tailored for the safe embedding of Electronic Patient Records (EPR) into Digital Imaging and Communications in Medicine (DICOM) pictures. The approach utilizes the Histogram of Oriented Gradients (HOG) with the Least Significant Bit (LSB) replacement technique, concentrating on regions of non-interest (RONI) inside DICOM pictures to preserve the integrity of the critical medical image material. The HOG edge detector recognizes these RONI regions, allowing the concealing of a hidden picture and metadata with little effect on the overall image quality. Furthermore, to augment security, the patient's RGB picture is encrypted using the Adaptive Nonlinear Chaotic-based SHA-256 (ANC-SHA-256) approach, supplemented with a digital signature using SHA-256 for each DICOM file. This digital signature, authenticated by a secret key, guarantees content integrity and authenticity, which is essential for preserving accuracy in sensitive medical information.

Comprehensive testing was conducted using several medical datasets—including MRI, CT, X-ray, and ultrasound pictures as cover images—to assess the visual quality and resilience of the proposed technique. Confidential photos from the LFW dataset were used, showing that the method maintains superior visual quality despite embedding. This approach achieves key visual quality criteria, including an average Peak Signal-to-Noise Ratio (PSNR) of 67.55, Normalized Cross-Correlation (NCC) of 0.9959, Structural Similarity Index (SSIM) of 0.9887, Universal Quality Index (UQI) of 0.9859, and an Average Pixel Error (APE) of 3.83. These measures underscore the approach's efficacy in preserving picture integrity and validate the method's capacity to endure diverse geometric assaults and histogram evaluations, demonstrating its robustness against prevalent tampering strategies. Moreover, in comparison to current state-of-the-art methods, the suggested methodology demonstrates superiority in metrics such as PSNR, Mean Squared Error (MSE), and SSIM across six categories of medical pictures, validating its enhanced visual quality and resilience. This secure embedding technology has considerable potential for telemedicine applications since it protects electronic patient records during internet transmission from distant sites while maintaining the visual integrity of medical pictures. The method proficiently satisfies the twin requirements of superior picture preservation and data security, making it a pragmatic and dependable alternative for medical information interchange. In a time of swiftly advancing digital healthcare, this technique is essential for safeguarding the security and precision of patient data, therefore fostering secure and dependable telemedicine procedures.

## References

- Aggarwal, N. K. (2021). International law and mental health evaluations at Guantanamo: Is medical repatriation a solution for most detainees? *International Journal of Law and Psychiatry*, 76, 101682. <https://doi.org/https://doi.org/10.1016/j.ijlp.2021.101682>
- Alhassan, A. L. (2023). Financial Health of Medical Schemes in South Africa. *Finance Research Letters*, 51. <https://doi.org/10.1016/j.frl.2022.103403>
- Alramadhan, M., Choe, J. H., Lee, J. H., Kim, J. H., & Kim, J. S. (2017). Propensity score-matched analysis of the endoscopic bilateral axillo-breast approach (BABA) versus conventional open thyroidectomy in patients with benign or intermediate fine-needle aspiration cytology results, a retrospective study. *International Journal of Surgery*, 48, 9–15.

- <https://doi.org/10.1016/j.ijisu.2017.09.077>
- Andritsos, D. A., & Tang, C. S. (2014). Linking process quality and resource usage: An empirical analysis. *Production and Operations Management*, 23(12), 2163–2177. <https://doi.org/10.1111/POMS.12249>
- Besharov, D. J., Barabashev, A., Baehler, K., & Klerman, J. A. (2013). Improving the Quality of Public Services: A Multinational Conference on Public Management. *Journal of Policy Analysis and Management*, 32(1), 204–210. <https://doi.org/10.1002/PAM.21672>
- Bhargava, A., Bhargava, M., Meher, A., Benedetti, A., Velayutham, B., Sai Teja, G., Watson, B., Barik, G., Pathak, R. R., Prasad, R., Dayal, R., Madhukeshwar, A. K., Chadha, V., Pai, M., Joshi, R., Menzies, D., & Swaminathan, S. (2023). Nutritional supplementation to prevent tuberculosis incidence in household contacts of patients with pulmonary tuberculosis in India (RATIONS): a field-based, open-label, cluster-randomised, controlled trial. *The Lancet*, 402(10402), 627–640. [https://doi.org/https://doi.org/10.1016/S0140-6736\(23\)01231-X](https://doi.org/https://doi.org/10.1016/S0140-6736(23)01231-X)
- Cai, W., Lou, Q., Fan, J., Yu, D., Shen, T., & Yu, J. (2019). Efficacy and Safety of Argon Laser Peripheral Iridoplasty and Systemic Medical Therapy in Asian Patients with Acute Primary Angle Closure: A Meta-Analysis of Randomized Controlled Trials. *Journal of Ophthalmology*, 2019. <https://doi.org/10.1155/2019/7697416>
- Caicedo, A., Zambrano, K., Sanon, S., & Gavilanes, A. W. D. (2021). Extracellular mitochondria in the cerebrospinal fluid (CSF): Potential types and key roles in central nervous system (CNS) physiology and pathogenesis. *Mitochondrion*, 58, 255–269. <https://doi.org/https://doi.org/10.1016/j.mito.2021.02.006>
- Chen, Y. C., Tsai, K. L., Hung, C. W., Ding, D. C., Chen, L. H., Chang, Y. L., Chen, L. K., & Chiou, S. H. (2011). Induced pluripotent stem cells and regenerative medicine. *Journal of Clinical Gerontology and Geriatrics*, 2(1), 1–6. <https://doi.org/10.1016/j.jcgg.2010.12.003>
- Gholami, M., Keshtvarz Hesam Abadi, A. M., Miladi, S., & Gholami, M. (2020). A systematic review of the factors affecting the growth of medical tourism in Iran. *International Journal of Travel Medicine and Global Health*, 8(1), 1–12.
- Go, A. S., Mozaffarian, D., Roger, V. L., Benjamin, E. J., Berry, J. D., Borden, W. B., Bravata, D. M., Dai, S., Ford, E. S., Fox, C. S., Franco, S., Fullerton, H. J., Gillespie, C., Hailpern, S. M., Heit, J. A., Howard, V. J., Huffman, M. D., Kissela, B. M., Kittner, S. J., ... Turner, M. B. (2013). Heart disease and stroke statistics-2013 update: A Report from the American Heart Association. *Circulation*, 127(1). <https://doi.org/10.1161/CIR.0B013E31828124AD>
- Hashmi, S., Richards, D., & Fedoroff, J. P. (2021). A descriptive analysis of sentencing decisions by the Canadian criminal justice system of people with intellectual disabilities convicted with sexual offences. *International Journal of Law and Psychiatry*, 78, 101730. <https://doi.org/https://doi.org/10.1016/j.ijlp.2021.101730>
- Hunter, N. D. (2018). 14 - Public Health Law II: Contemporary Threats (N. D. B. T.-T. L. of E. (Second E. Hunter (Ed.); pp. 245–271). Butterworth-Heinemann. <https://doi.org/https://doi.org/10.1016/B978-0-12-804275-5.00014-0>
- Laub, J. A. (1999). Assessing the servant organization; Development of the Organizational Leadership Assessment (OLA) model. *Dissertation Abstracts International*,. *Procedia - Social and Behavioral Sciences*.
- Lewis, O., & Campbell, A. (2017). Violence and abuse against people with disabilities: A comparison of the approaches of the European Court of Human Rights and the United Nations Committee on the Rights of Persons with Disabilities. *International Journal of Law and Psychiatry*, 53, 45–58. <https://doi.org/https://doi.org/10.1016/j.ijlp.2017.05.008>



- Li, J., Wu, Y., & Xiao, J. J. (2020). The impact of digital finance on household consumption: Evidence from China. *Economic Modelling*, 86, 317–326. <https://doi.org/10.1016/j.econmod.2019.09.027>
- Park, S. J., Lim, H. S., Lee, K., & Yoo, S. J. (2018). Green Tobacco Sickness Among Tobacco Harvesters in a Korean Village. *Safety and Health at Work*, 9(1), 71–74. <https://doi.org/10.1016/j.shaw.2017.06.007>
- Qian, M., & Jiang, J. (2022). COVID-19 and social distancing. In *Journal of Public Health (Germany)* (Vol. 30, Issue 1). <https://doi.org/10.1007/s10389-020-01321-z>
- Qiu, L., Yu, R., Hu, F., Zhou, H., & Hu, H. (2023). How can China's medical manufacturing listed firms improve their technological innovation efficiency? An analysis based on a three-stage DEA model and corporate governance configurations. *Technological Forecasting and Social Change*, 194, 122684. <https://doi.org/https://doi.org/10.1016/j.techfore.2023.122684>
- Rajak, M., & Shaw, K. (2019). Evaluation and selection of mobile health (mHealth) applications using AHP and fuzzy TOPSIS. *Technology in Society*, 59. <https://doi.org/10.1016/j.techsoc.2019.101186>
- Tang, K. H. D. (2022). Movement control as an effective measure against Covid-19 spread in Malaysia: an overview. In *Journal of Public Health (Germany)* (Vol. 30, Issue 3). <https://doi.org/10.1007/s10389-020-01316-w>
- Van Hout, M. C., Kaima, R., Mhango, V., Kewley, S., & Mariniello, T. (2023). Judicialisation of the mentally ill and/or mentally incapacitated in the Malawi criminal justice system: Gaps and flaws of human rights protection. *Forensic Science International: Mind and Law*, 4, 100121. <https://doi.org/https://doi.org/10.1016/j.fsimpl.2023.100121>
- Wang, M., Chen, H., Yang, B., Zhao, X., Hu, L., Cai, Z., Huang, H., & Tong, C. (2017). Toward an optimal kernel extreme learning machine using a chaotic moth-flame optimization strategy with applications in medical diagnoses. *Neurocomputing*, 267, 69–84. <https://doi.org/10.1016/j.neucom.2017.04.060>
- Xu, C., Cassatella, D., van der Sloot, A. M., Quinton, R., Hauschild, M., De Geyter, C., Flück, C., Feller, K., Bartholdi, D., Nemeth, A., Halperin, I., Pekic Djurdjevic, S., Maeder, P., Papadakis, G., Dwyer, A. A., Marino, L., Favre, L., Pignatelli, D., Niederländer, N. J., ... Pitteloud, N. (2018). Evaluating CHARGE syndrome in congenital hypogonadotropic hypogonadism patients harboring CHD7 variants. *Genetics in Medicine*, 20(8), 872–881. <https://doi.org/10.1038/gim.2017.197>
- Yang, Q., Cogswell, M. E., Dana Flanders, W., Hong, Y., Zhang, Z., Loustalot, F., Gillespie, C., Merritt, R., & Hu, F. B. (2012). Trends in cardiovascular health metrics and associations with all-cause and CVD mortality among us adults. *JAMA - Journal of the American Medical Association*, 307(12), 1273–1283. <https://doi.org/10.1001/JAMA.2012.339>
- Yazdanpanah, N., & Rezaei, N. (2022). Autoimmune complications of COVID-19. In *Journal of Medical Virology* (Vol. 94, Issue 1). <https://doi.org/10.1002/jmv.27292>
- Ye, F., Sun, Z., Yang, D., Wang, H., & Xi, X. (2021). Corticomuscular coupling analysis based on improved LSTM and transfer entropy. *Neuroscience Letters*, 760, 136012. <https://doi.org/10.1016/J.NEULET.2021.136012>